Four approaches to determine masonry strength domain

Gabriele Milani MEng, PhD
Associate Professor, Department of Architecture, Built Environment and Construction Engineering A.B.C., Technical University of Milan, Milan, Italy

1. Introduction

In recent years, there has been a steady interest focused on the interpretation of the mechanical behaviour of masonry at failure (Cecchi *et al.*, 2007; Gilbert *et al.*, 2006; Milani *et al.*, 2006a, 2006b, 2006c; Portioli *et al.*, 2013, 2014; Restrepo-Vélez *et al.*, 2014). The aim is to always provide reliable and efficient tools for fast estimates of brickwork behaviour near collapse.

There are two main approaches widely used in the literature for the constitutive description of masonry, usually known as macro- and micro-modelling.

Macro-modelling (Lourenço *et al.*, 1997; Shieh-Beygi and Pietruszczak, 2008) does not make any distinction between masonry units (bricks, blocks, stones etc.) and joints, averaging the effect of mortar through the formulation of a fictitious continuous material. Despite this, macro-modelling is – at a first glance – the most straightforward from an engineering point of view, because it makes it possible to apply the rough discretisation needed for actual large-scale computations, it usually requires many mechanical parameters to be set, which are obtained by best fitting of costly experimental campaign on masonry wallettes. However, the analysis of a different

masonry material or texture would require a new calibration of the model parameters, with the subsequent need to perform new experimentations.

The alternative micro-modelling approach (Lotfi and Shing, 1994; Lourenço and Rots, 1997) consists of separately representing mortar joints and units. In some cases, reasonable simplifications have been introduced; for example, utilising zero-thickness interfaces for the joints. Nevertheless, a drawback of this approach is related to the need of separately modelling units and mortar, with a consequent numerical effort proportional to the number of bricks present in the structure, which limits its applicability to small panels.

Homogenisation (de Buhan and de Felice, 1997; Luciano and Sacco, 1997; Milani *et al.*, 2006a, 2006b, 2006c; Pegon and Anthoine, 1997) represents a fair compromise between micro- and macro-modelling, because it allows the necessary rough discretisation at a structural level, but at the same time representing in detail what happens at the meso-scale on each Gauss point. The practical advantage of homogenisation stands therefore in the fact that only the knowledge of constituent materials (brick and mortar) mechanical parameters are required to provide an estimate of masonry average behaviour

to use at a structural level. In addition, texture properties are not needed anymore in large-scale computations and meshes that do not depend on brick size may be used.

The major limitation of homogenisation is related to non-linear finite-element (FE) computations, because a continuous interaction between meso- and macro-scale is needed in the non-linear range. The practical translation of this issue is a huge computational effort, since the field problem has to be solved numerically for each loading step, in all Gauss points.

For the above reasons, limit analysis combined with homogenisation technique still seems to be one of the most powerful and direct structural analysis methods to provide reliable and fast results at collapse. Such an approach requires only a reduced number of material parameters and allows the avoidance of independent modelling of units and mortar. In addition, it provides limit multipliers of loads, failure mechanisms and, at least on critical sections, the stress distribution at collapse. It belongs to the so-called 'direct' methods, because the results are obtained in a single step solving a suitable optimisation problem. Different homogenisation models have been recently proposed in the technical literature for the evaluation of homogenised strength domains for masonry walls in-plane loaded (de Buhan and de Felice, 1997; Milani et al., 2006a, 2006b).

The paper is aimed at critically reviewing some of the most effective models already available, with a comparison of their numerical performance within some applications of technical interest.

In particular, four different strategies for the evaluation of the homogenised strength domain of running bond masonry in-plane loaded are discussed and critically compared. Under the assumption of mortar and bricks obeying a rigid plastic behaviour with associated flow rule, and within basic assumptions of the homogenisation theory (such as periodicity and anti-periodicity of the local velocity field and micro-stress, respectively), an estimation of masonry macroscopic strength domain is possible by means of the application of both the classic upper and lower bound theorems of limit analysis on the chosen elementary cell (Suquet, 1983). In particular, the lower bound approach requires the imposition of micro-stress equilibrium, admissibility as well as anti-periodicity and allows obtaining lower bound estimates of the actual homogenised failure surface by means of the constrained maximisation of the homogenised internal actions. The upper bound approach, dually, requires dealing with kinematically admissible velocity fields (i.e. obeying associated flow rules), with periodicity conditions applied at the boundary of the elementary cell, allowing upper bound estimates of the actual homogenised failure surface by means of the constrained minimisation of the total

internal power dissipation. In both cases, the mechanical problem translates mathematically into (non)-linear programming, where the total number of optimisation unknowns is reduced. Four different models recently proposed by the author, two lower bounds and two upper bounds, are analysed and critically compared. The first lower bound model (Milani et al., 2006a, 2006b), model I, subdivides the elementary cell into a few rectangular sub-domains, where the micro-stress field is expanded using polynomial expressions. In the second lower bound procedure (Milani, 2011a, 2011b), model II, joints are reduced to interfaces and bricks are subdivided into a few constant stress triangular elements (CST). In this latter case, closed-form estimates of the homogenised strength domain may be determined in some special cases. The third procedure (Cecchi and Milani, 2008; Milani, 2009), model III, is an upper bound heuristic approach also known as 'compatible identification', with joints reduced to interfaces and bricks assumed infinitely resistant. The periodic velocity field results as a linear combination of elementary deformation modes a priori applied on the elementary cell. The last model, model IV, is a kinematically admissible procedure based on the so-called method of cells (MoC) (Aboudi, 1991; Milani and Taliercio, 2015; Taliercio, 2014), where the elementary cell is subdivided into six rectangular sub-cells with pre-assigned polynomial fields of periodic velocity. Models I and IV have the advantage that the reduction of joints to interfaces is not required. The second approach, albeit reduces joints to interfaces with frictional behaviour, still allows considering failure inside bricks. The third model is the most straightforward, but is reliable only in case of thin joints and strong blocks. A critical comparison of pros and cons of all models is discussed, with reference to realistic benchmarks.

2. Homogenisation theory: basic assumptions

Masonry is a composite material usually made of units bonded with mortar joints. In most cases of building practice, units and mortar are periodically arranged. Such periodicity gives the possibility to consider an entire wall Ω as the repetition of a representative element of volume Y representative element of volume (REV) or elementary cell. Y contains all the information necessary for describing completely the macroscopic behaviour of Ω. If a running bond pattern is considered, it can be easily checked that the elementary cell is rectangular.

For periodic arrangements of units and mortar, homogenisation techniques can be used both in the elastic and inelastic range, taking into account the micro-structure only at a cell level. This leads to a significant simplification of the numerical models adopted for studying entire walls, especially for the inelastic case.

The basic idea of the homogenisation procedure consists in introducing averaged quantities representing the macroscopic strain and stress tensors (respectively $\boldsymbol{E}$ and $\boldsymbol{\Sigma}$), as follows

1.
$$\boldsymbol{E} = <\boldsymbol{\varepsilon}> = \frac{1}{A}\int_Y \boldsymbol{\varepsilon}\,\mathrm{d}Y$$
$$\boldsymbol{\Sigma} = <\boldsymbol{\sigma}> = \frac{1}{A}\int_Y \boldsymbol{\sigma}\,\mathrm{d}Y$$

where A stands for the area of the elementary cell, $\boldsymbol{\varepsilon}$ and $\boldsymbol{\sigma}$ stand for the local quantities (strains – or strain rates in limit analysis – and stresses, respectively) and $<*>$ is the averaging operator.

Periodicity conditions are imposed on the stress field $\boldsymbol{\sigma}$ and the displacement (or velocity in limit analysis) field $\boldsymbol{u}$, and are given by

2.
$$\begin{cases} \boldsymbol{u} = \boldsymbol{E}\boldsymbol{y} + \boldsymbol{u}^{\mathrm{per}}, \ \ \boldsymbol{u}^{\mathrm{per}} \ \text{on} \ \ \partial Y \\ \boldsymbol{\sigma}\boldsymbol{n}, \ \ \text{anti}-\text{periodic on} \ \ \partial Y \end{cases}$$

where $\boldsymbol{u}^{\mathrm{per}}$ stands for a periodic displacement (velocity) field.

Let $\boldsymbol{f}_{\mathrm{m}}$, $\boldsymbol{f}_{\mathrm{b}}$ and $\boldsymbol{f}_{\mathrm{hom}}$ denote, respectively, the strength domains of the mortar, of the units and of the homogenised macroscopic material. It has been shown by Suquet (1983) that the $\boldsymbol{f}_{\mathrm{hom}}$ domain of the equivalent continuum is defined in the space of the macroscopic stresses as follows

3.
$$\boldsymbol{f}_{\mathrm{hom}} = \left\{ \boldsymbol{\Sigma} \,\middle|\, \begin{cases} \boldsymbol{\Sigma} = <\boldsymbol{\sigma}> = \frac{1}{A}\int_Y \boldsymbol{\sigma}\,\mathrm{d}Y & (a) \\ \mathrm{div}\,\boldsymbol{\sigma} = \boldsymbol{0} & (b) \\ [[\boldsymbol{\sigma}]]\boldsymbol{n}^{\mathrm{int}} = \boldsymbol{0} & (c) \\ \boldsymbol{\sigma}\boldsymbol{n}, \ \ \text{anti-periodic on} \ \ \partial Y & (d) \\ \boldsymbol{\sigma}(\boldsymbol{y}) \in \boldsymbol{f}_{\mathrm{m}}, \ \ \forall \boldsymbol{y} \in Y^{\mathrm{m}} \ \ \boldsymbol{\sigma}(\boldsymbol{y}) \in \boldsymbol{f}_{\mathrm{b}}, \ \ \forall \boldsymbol{y} \in Y^{\mathrm{b}} & (e) \end{cases} \right\}$$

Here, $[[\boldsymbol{\sigma}]]$ is the jump of micro-stresses across any discontinuity surface of normal $\boldsymbol{n}^{\mathrm{int}}$. Conditions 3a and 3d are derived from periodicity, condition 3b imposes the micro-equilibrium and condition 3e represents the yield criteria for the components (brick and mortar).

A dual kinematic definition of $\boldsymbol{f}_{\mathrm{hom}}$, also due to Suquet (1983), can be derived through the support function $\pi^{\mathrm{hom}}(\boldsymbol{D})$ as follows

4.
$$\boldsymbol{f}_{\mathrm{hom}} = \left\{ \boldsymbol{\Sigma} \,\middle|\, \begin{cases} \boldsymbol{\Sigma} : \boldsymbol{D} \le \pi^{\mathrm{hom}}(\boldsymbol{D}) \ \ \forall \boldsymbol{D} \\ \pi^{\mathrm{hom}}(\boldsymbol{D}) = \inf_{\boldsymbol{v}}\left\{ P(\boldsymbol{v}) \,\middle|\, \boldsymbol{D} = \frac{1}{2\Gamma}\int_{\partial Y = \Gamma} (\boldsymbol{v}\otimes\boldsymbol{n} + \boldsymbol{n}\otimes\boldsymbol{v})\mathrm{d}S \right\} \\ P(\boldsymbol{v}) = \int_Y \pi(\boldsymbol{d})\mathrm{d}Y + \int_S \pi([[\boldsymbol{v}]];\boldsymbol{n})\mathrm{d}S \end{cases} \right\}$$

where $\boldsymbol{v} = \boldsymbol{D}\boldsymbol{y} + \boldsymbol{v}^{\mathrm{per}}$ is the microscopic velocity field; $\boldsymbol{v}^{\mathrm{per}}$ is a periodic velocity field; $\boldsymbol{d}$ and $\boldsymbol{D}$ are, respectively, the microscopic and macroscopic strain rate fields; S is any discontinuity surface of $\boldsymbol{v}$ in Y; $\boldsymbol{n}$ is the normal to S; $\pi([[\boldsymbol{v}]];\boldsymbol{n}) = 1/2([[\boldsymbol{v}]]\otimes\boldsymbol{n} + \boldsymbol{n}\otimes[[\boldsymbol{v}]])$; and $\pi(\boldsymbol{d}) = \max_{\boldsymbol{\sigma}}\{\boldsymbol{\sigma}:\boldsymbol{d}; \ \boldsymbol{\sigma} \in S(\boldsymbol{y})\}$.

3. Model I: polynomial expansion of the micro-stress field

In Milani *et al.* (2006a, 2006b), a model based on the assumption of equilibrated polynomial stress fields inside the unit cell is presented. Essentially, the approach relies on a rough subdivision of the unit cell by means of rectangular sub-domains, where a polynomial interpolation of the stress field is a priori given. Equilibrium inside each element and at the interface between contiguous elements, as well as anti-periodicity conditions are imposed. In this way, the micro-stress field is anti-periodic and auto-equilibrated, fully complying constraints 3b–d.

As shown in Figure 1, one-fourth of the REV is subdivided into nine geometrical elementary entities (subdomains), so that the whole cell is sub-divided into 36 sub-domains.

For each sub-domain, polynomial distributions of degree (m) are a priori assumed for the stress components. The generic ijth component can be written as follows

5.
$$\sigma_{ij}^{(k)} = X(\boldsymbol{y})\boldsymbol{S}_{ij}^{\mathrm{T}}, \quad \boldsymbol{y} \in Y^k$$

where $X(\boldsymbol{y}) = [1 \ y_1 \ y_2 \ y_1^2 \ y_1 \ y_2 \ y_2^2 \ldots]$; $\boldsymbol{S}_{ij} = [S_{ij}^{(1)} \ S_{ij}^{(2)} \ S_{ij}^{(3)} \ S_{ij}^{(4)} \ S_{ij}^{(5)} \ S_{ij}^{(6)} \ldots]$ is a vector of length $\tilde{N} = ((m+1) + (m+2)/2)$ representing the unknown stress parameters; and Y^k represents the kth sub-domain.

The imposition of equilibrium with zero body forces inside every sub-domain, the continuity of the stress vector on interfaces and anti-periodicity of $\boldsymbol{\sigma}\boldsymbol{n}$ allows for a strong reduction of the total number of independent stress parameters.

In particular, equilibrium has to be imposed everywhere inside each sub-domain, that is, $\sigma_{ij,j}(x, y) = 0$, $i = 1, 2 \ \forall(x, y) \in$ sub-domain. Since $\sigma_{ij}(x, y)$ is a polynomial expression of degree (m), a linear combination of its derivatives (div $\boldsymbol{\sigma}$) is a polynomial of degree ($m-1$). This leads to write ($2N$) linear independent equations in the stress coefficients, where $N = ((m-1)^2/2) + (3(m-1)/2) + 1 = (m(m+1)/2)$.

A further reduction of the total unknowns is obtained a priori imposing the continuity of the stress vector on internal
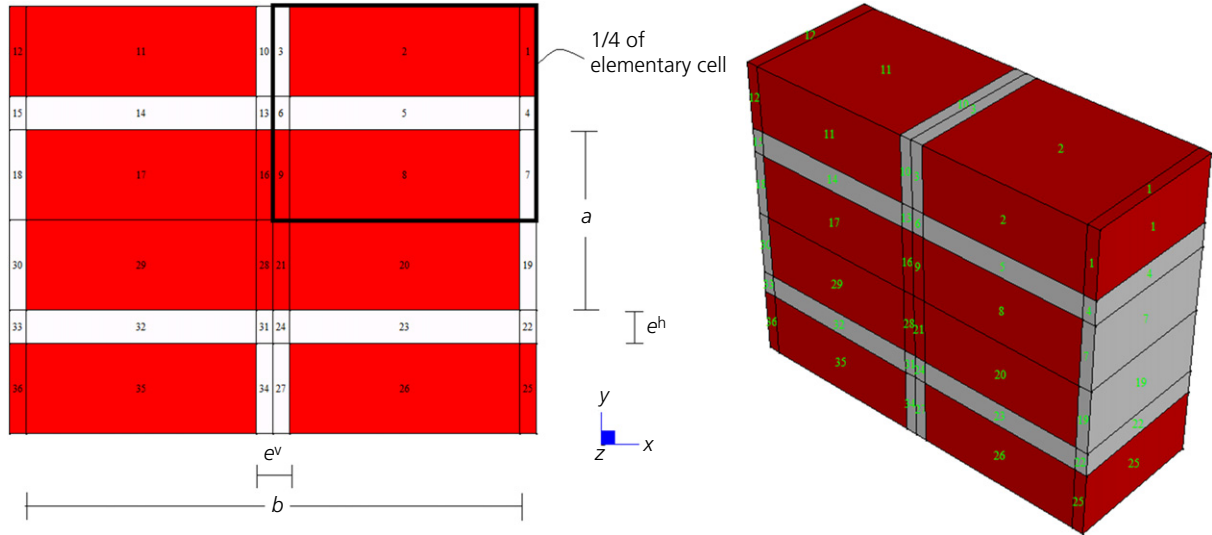
Figure 1. Subdivision in sub-domains adopted: left: subdivision and geometrical characteristics of one-fourth of the elementary cell; right: subdivision into 36 sub-domains for the entire cell

interfaces ($\sigma_{ij}^{(k)}n_j + \sigma_{ij}^{(r)}n_j = 0$; $i = 1, 2$) for every (k) and (r) contiguous sub-domains with a common interface of normal $\boldsymbol{n}$ (Figure 2(a)). Being $\boldsymbol{\sigma n}$ polynomial expressions of degree (m) in the abscissa s of the interface, other $2N'$ equations (where $N' = m + 1$) in $\hat{\boldsymbol{S}}^{(k)}$ and $\hat{\boldsymbol{S}}^{(r)}$ for each k–r interface can be written.

Finally, anti-periodicity of $\boldsymbol{\sigma n}$ on ∂V requires $2N'$ additional equations per pair of external faces (m)(n) (Figure 2(b)), that is, it should be imposed that stress vectors $\boldsymbol{\sigma n}$ are opposite on

opposite sides of ∂V

6. $\hat{\boldsymbol{X}}_{ij}^{(m)}(\boldsymbol{y})\hat{\boldsymbol{S}}^{(m)}\boldsymbol{n}_1 = -\hat{\boldsymbol{X}}_{ij}^{(n)}(\boldsymbol{y})\hat{\boldsymbol{S}}^{(n)}\boldsymbol{n}_2$

where $\boldsymbol{n}^{(m)}$ and $\boldsymbol{n}^{(n)}$ are oriented vectors of the external faces of the paired sub-domains (m)(n).

Again $\boldsymbol{\sigma n}$ on ∂V is a polynomial expression of degree (m) in the abscissa s of the external edge of the sub-domain.
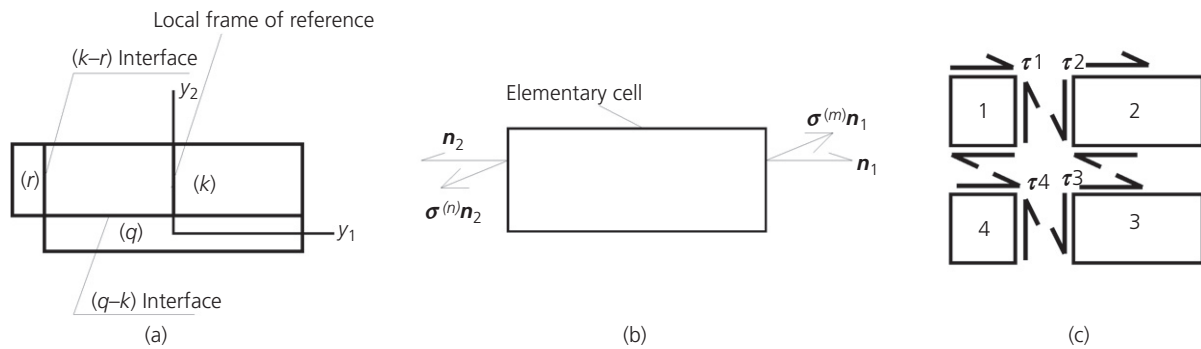

Figure 2. (a) contiguous sub-domains, geometry and frame of reference of the sub-domains with vertical/horizontal interfaces between adjacent sub-domains; (b) anti-periodicity conditions on the unit cell; and (c) linear dependence of some equilibrium equations

The equations written in order to satisfy internal equilibrium, equilibrium on interfaces and anti-periodicity of the stress vector lead to a system of equations in the form $\mathbf{A}S = 0$, where S is the vector of total stress parameters. Nevertheless, not all the rows of this system are linearly independent. This can be easily shown if four generic rectangular elements with four common interfaces and subjected only to constant non-zero shear stress are considered, as reported in Figure 2(c). Internal equilibrium is a priori satisfied, whereas four equations for ensuring equilibrium on interfaces have to be written. Nevertheless, only three of these four equations are linearly independent.

The detection of linearly dependent equations is automatically checked with a 'for' cycle, evaluating the rank of the sub-matrices $\mathbf{A}_i$, where $\mathbf{A}_i$ collects the first i-rows of $\mathbf{A}$.

After some trivial assemblage operations on the local variables (again handled automatically), it is possible to write the stress vector inside every sub-domain as follows

7. $$\tilde{\boldsymbol{\sigma}}^{(k)} = \tilde{\mathbf{X}}^{(k)}(\boldsymbol{y})\tilde{\boldsymbol{S}}, \quad k = 1,\dots,k^{\max}$$

where $\tilde{\boldsymbol{\sigma}}^{(k)}$ is the stress vector inside the kth sub-domain; $\tilde{\mathbf{X}}^{(k)}(\boldsymbol{y})$ is a $3 \times N_{\mathrm{un}}$ matrix that contains only geometrical coefficients; its elements are polynomial forms in the microscopic coordinate $\boldsymbol{y}$; $\tilde{\boldsymbol{S}}$ is the vector (of length N_{un}) of the total stress parameters unknown.

Four different models of increasing accuracy (P0, P2, P3, P4) have been obtained (Milani *et al.*, 2006a, 2006b, 2006c), progressively increasing the degree of the polynomial expansion. It can be shown that the stress unknown independent parameters are 69, 39, 29 and 8 for models P4, P3, P2 and P0, respectively.

Micro-stress fields 7 are equilibrated and anti-periodic, but not necessarily admissible. Condition 3d has to be checked in every point of the cell, or alternatively where the stress status is the maximum. This is feasible only for polynomial expressions with degree 0 and 1. Alternatively, in Milani *et al.* (2006a, 2006b, 2006c), a collocation method is adopted, enforcing, in every sub-domain, the admissibility condition in a regular grid of 'nodal points' with step $r \times q$. In Milani *et al.* (2006a), it is shown how even coarse grids (3×3) provide quite reliable results.

To evaluate a point of the homogenised failure surface solving problem 3, a direction $\boldsymbol{n}_{\Sigma}$ in the homogenised stress space $[\Sigma_{xx}\Sigma_{yy}\Sigma_{xy}]^{\mathrm{T}}$ is a priori chosen. Traditionally, principal stresses $\Sigma_{\mathrm{h}} - \Sigma_{\mathrm{v}}$ are applied up to failure on wallettes, with an orientation ϑ of the bed joint with respect to Σ_{h}.

Under such assumptions, the failure multiplier Λ is estimated by means of the following linear programming (LP) problem

$\max\{\Lambda\}$

8.
$$
\begin{cases}
\Lambda\boldsymbol{n}_{\Sigma} = \dfrac{1}{Y}\sum_k \displaystyle\int_Y \tilde{\mathbf{X}}^{(k)}(\boldsymbol{y})\tilde{\boldsymbol{S}}\,\mathrm{d}Y \\[2mm]
\boldsymbol{y}^j \equiv \text{nodal point} \\[2mm]
\tilde{\boldsymbol{\sigma}}^j = \tilde{\mathbf{X}}^{(k)}(\boldsymbol{y}^j)\tilde{\boldsymbol{S}} \\[2mm]
\tilde{\boldsymbol{\sigma}}^j \in \boldsymbol{f}_k, \quad j = 1,\dots,rq, \quad k = 1,\dots,4k^{\max} \\[2mm]
\boldsymbol{n}_{\Sigma,1} = \dfrac{1}{2}\left(\cos(\psi)(1 + \cos(2\vartheta)) + \sin(\psi)(1 - \cos(2\vartheta))\right) \\[2mm]
\boldsymbol{n}_{\Sigma,2} = \dfrac{1}{2}\left(\cos(\psi)(1 - \cos(2\vartheta)) + \sin(\psi)(1 + \cos(2\vartheta))\right) \\[2mm]
\boldsymbol{n}_{\Sigma,3} = \dfrac{1}{2}\left(\cos(\psi)\cos(2\vartheta) - \sin(\psi)\cos(2\vartheta)\right)\tan(2\vartheta)
\end{cases}
$$

where, apart from the symbols already introduced, $\boldsymbol{f}_k$ is the kth sub-domain yield criterion. ψ denotes the loading angle, given by $\tan(\psi) = \Sigma_{\mathrm{v}}/\Sigma_{\mathrm{h}}$ (Σ_{v} and Σ_{h} are the principal homogenised internal actions). ϑ denotes the angle between Σ_{h} and the bed joint orientation.

It is interesting to note that, from problem 3, the membrane strength components are $\Sigma_{xx} = \Lambda\boldsymbol{n}_{\Sigma,1}$, $\Sigma_{yy} = \Lambda\boldsymbol{n}_{\Sigma,2}$ and $\Sigma_{xy} = \Lambda\boldsymbol{n}_{\Sigma,3}$.

4.   Model II: equilibrated model with joints reduced to interfaces and CST discretisation of the bricks

In Milani (2011a, 2011b), an equilibrated model relying on the subdivision of the unit cell into 24 CSTs and joints reduced to interfaces is presented. In Milani (2011a), it is also shown that, in particular cases, due to the very limited number of optimisation variables involved, the model can be handled also without the assistance of a computer.

Joints are reduced to interfaces with zero thickness and blocks are discretised by means of a coarse mesh constituted by constant stress (CST) elements (Figure 3). The choice of meshing one-fourth of the brick through at least three triangular elements is due to the need of reproducing the presence of shear stress in the bed joint (element 2 in Figure 3) in horizontal stretching. All the non-linearity in the REV is concentrated exclusively on interfaces between the adjoining elements both on the brick and the joint. Brick–brick interfaces allow, at least in principle, the reproduction of blocks failure. The six CST elements used for the discretisation of the upper-right one-fourth of the REV are indicated in Figure 3 as 1, 2, 3, 1′, 2′ and 3′.
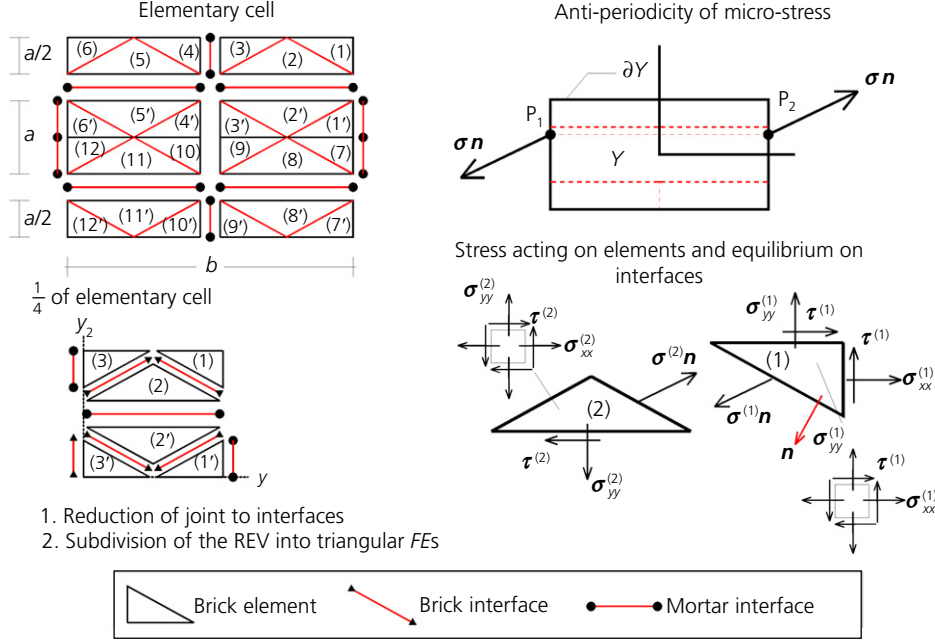
Figure 3. The micro-mechanical model proposed. Subdivision of the REV into 24 CST triangular elements (and one-fourth into six elements), anti-periodicity of the micro-stress field and equilibrium on interfaces

From here onwards, the superscript $^{(n)}$ will indicate any stress component belonging to the nth element. Accordingly, assuming the wall to undergo plane-stress conditions, the Cauchy stress tensor in the nth CST element, $\boldsymbol{\sigma}^{(n)}$, is characterised by the three non-vanishing components $\sigma_{xx}^{(n)}$ (horizontal stress), $\sigma_{yy}^{(n)}$ (vertical stress) and $\sigma_{xy}^{(n)}$ (shear stress, also denoted by $\boldsymbol{\tau}^{(n)}$).

Neglecting the body forces, equilibrium within any element is a priori satisfied, div$\boldsymbol{\sigma}=\mathbf{0}$. On the contrary, two equality constraints involving stress components in adjoining triangular elements have to be prescribed at any internal interface. For instance, when dealing with the interface between elements 1 and 2, the stress vector must be continuous when passing from an element to the other. It can be shown that stress components of elements 1 and 2 are linked by the following two equations

9.

$$\sigma_{xx}^{(2)} = \sigma_{xx}^{(1)} + m^{-1}\left(\boldsymbol{\tau}^{(1)} - \boldsymbol{\tau}^{(2)}\right)$$
$$\sigma_{yy}^{(2)} = \sigma_{yy}^{(1)} + m\left(\boldsymbol{\tau}^{(1)} - \boldsymbol{\tau}^{(2)}\right)$$

having denoted, as in de Buhan and de Felice (1997), with m^{-1} being the ratio between the semi-length and the height of

the brick ($m^{-1}=b/2a$). Similar equations must be written at all the remaining interfaces, which are globally 28. Fifty-six equilibrium equations at the interfaces are obtained. Seventy-three are the unknowns of the problem, including 72 stress components (three for each triangular element), and the load multiplier Λ.

Anti-periodicity constrains for the stress vector are prescribed on the couples of triangles 1–6, 7–12, 1′–6′, 7′–12′, 1–7, 3–9′, 4–10′, 6–12′, leading to additional 16 equalities. For instance, referring to couple 1–6, stress anti-periodicity amounts at setting

10.

$$\sigma_{xx}^{(1)} = \sigma_{xx}^{(6)}$$
$$\boldsymbol{\tau}^{(1)} = \boldsymbol{\tau}^{(6)}$$

Not all the equations are, however, linearly independent. In particular, it can be shown that the corner elements 1, 6, 7′ and 12′ provide four linearly dependent equations on shear.

To summarise, the optimisation problem involves 73 unknowns, 68 linearly independent equations and a set of inequality constraints representing the yield conditions at the

interfaces and involving unknown stress components. The objective function, in the framework of the lower bound theorem of limit analysis, is simply the load multiplier Λ.

To estimate a single point of the homogenised yield domain, it is thus necessary to solve the following LP problem

11. $\max \Lambda$ s.t.
$$
\begin{cases}
\Lambda\alpha = \dfrac{\sum_{i=1}^{24} \boldsymbol{\sigma}_{xx}^{(i)} A_i}{2ab} \\[2mm]
\Lambda\beta = \dfrac{\sum_{i=1}^{24} \boldsymbol{\sigma}_{yy}^{(i)} A_i}{2ab} \\[2mm]
\Lambda\gamma = \dfrac{\sum_{i=1}^{24} \boldsymbol{\tau}^{(i)} A_i}{2ab} \\[2mm]
\mathbf{A}_{\mathrm{eq}}^{I}\mathbf{X} = \mathbf{b}_{\mathrm{eq}}^{I} \\[1mm]
\mathbf{A}_{\mathrm{eq}}^{\mathrm{ap}}\mathbf{X} = \boldsymbol{b}_{\mathrm{eq}}^{\mathrm{ap}} \\[1mm]
\mathbf{f}_{E}^{i}\left(\boldsymbol{\sigma}_{xx}^{(i)}, \boldsymbol{\sigma}_{yy}^{(i)}, \boldsymbol{\tau}^{(i)}\right) \leq 0, \ i = 1, \ldots, 24 \\[1mm]
\boldsymbol{f}_{I}^{i}\left(\boldsymbol{\sigma}_{I}^{(i)}, \boldsymbol{\tau}_{I}^{(i)}\right) \leq 0, \ i = 1, \ldots, 32
\end{cases}
$$

The symbols used in Equation 11 have the following meaning.

■ α, β and γ indicate the components of the unit vector $\boldsymbol{n}_\Sigma$, in the homogenised in-plane stress space and already defined for model I. The solution of the optimisation problem 11 allows a point on the homogenised failure surface to be determined, having coordinates $\Sigma_{xx} = \alpha\Lambda$, $\Sigma_{yy} = \beta\Lambda$; and $\Sigma_{xy} = \gamma\Lambda$.

■ A_i is the area of the ith element ($ab/8$ or $ab/16$).

■ $\mathbf{X}$ is a 73×1 array, gathering all the LP problem unknowns (element stress components and collapse multiplier). More precisely, the stress components in any element (i) are assembled into $\mathbf{X}$ as $\mathbf{X}(3(i-1)+1) = \boldsymbol{\sigma}_{xx}^{(i)}$, $\mathbf{X}(3(i-1)+2) = \boldsymbol{\sigma}_{yy}^{(i)}$ and $\mathbf{X}(3(i-1)+3) = \tau^{(i)}$, whereas $\mathbf{X}(73) = \Lambda$.

■ $\mathbf{A}_{\mathrm{eq}}^{I}\mathbf{X} = \mathbf{b}_{\mathrm{eq}}^{I}$ is a set of linear equations collecting equilibrium constraints on all the interfaces. $\mathbf{A}_{\mathrm{eq}}^{I}$ is a 56×73 matrix and $\mathbf{b}_{\mathrm{eq}}^{I}$ is a 56×1 array with entries equal to zero. To show practically how matrix $\mathbf{A}_{\mathrm{eq}}^{I}$ is populated, let us consider the two equilibrium equations to be imposed at the interface between elements 1 and 2, – that is Equation 9. Assuming that Equation 9 corresponds to the first two rows of matrix $\mathbf{A}_{\mathrm{eq}}^{I}$, all the entries in these rows are equal to zero except for $\mathbf{A}_{\mathrm{eq}}^{I}(1, 1) = 1$, $\mathbf{A}_{\mathrm{eq}}^{I}(1, 3) = m^{-1}$ $\mathbf{A}_{\mathrm{eq}}^{I}(1, 4) = -1$, $\mathbf{A}_{\mathrm{eq}}^{I}(1, 6) = -m^{-1}$, $\mathbf{A}_{\mathrm{eq}}^{I}(2, 2) = 1$, $\mathbf{A}_{\mathrm{eq}}^{I}(2, 3) = m$, $\mathbf{A}_{\mathrm{eq}}^{I}(2, 5) = -1$, $\mathbf{A}_{\mathrm{eq}}^{I}(2, 6) = -m$.

■ $\mathbf{A}_{\mathrm{eq}}^{\mathrm{ap}}\mathbf{X} = \boldsymbol{b}_{\mathrm{eq}}^{\mathrm{ap}}$ collects the anti-periodicity conditions and it is therefore a set of 16 equations (some of them linearly dependent). Thus, $\mathbf{A}_{\mathrm{eq}}^{\mathrm{ap}}$ is a 16×73 matrix and $\boldsymbol{b}_{\mathrm{eq}}^{\mathrm{ap}}$ is a 16×1 array with entries equal to zero. To show practically how matrix $\mathbf{A}_{\mathrm{eq}}^{\mathrm{ap}}$ is populated, let us consider the two homologous elements 1 and 6, where anti-periodicity holds at the vertical boundaries, Equation 10. Assume that Equation 10 corresponds to the first two rows of matrix $\mathbf{A}_{\mathrm{eq}}^{\mathrm{ap}}$, hence $\mathbf{A}_{\mathrm{eq}}^{\mathrm{ap}}(1, 1) = 1$, $\mathbf{A}_{\mathrm{eq}}^{\mathrm{ap}}(1, 16) = -1$, $\mathbf{A}_{\mathrm{eq}}^{\mathrm{ap}}(2, 3) = 1$, $\mathbf{A}_{\mathrm{eq}}^{\mathrm{ap}}(2, 18) = -1$.

■ $\boldsymbol{f}_{E}^{i}(\sigma_{xx}^{(i)}, \sigma_{yy}^{(i)}, \boldsymbol{\tau}^{(i)}) \leq 0$ is a set of (possibly) non-linear inequality constraints representing the failure surface adopted for the ith element.

■ $\boldsymbol{f}_{I}^{i}(\sigma_{I}^{(i)}, \boldsymbol{\tau}_{I}^{(i)}) \leq 0 \ \forall i = 1, \ldots, 32$ plays the role of $\boldsymbol{f}_{E}^{i}$ at the interfaces, with $\sigma_{I}^{(i)}$ and $\boldsymbol{\tau}_{I}^{(i)}$ indicating the normal and shear stress acting on the ith interface, respectively. Two typologies of interfaces are present in the model, namely brick-to-brick interfaces and mortar joints.

In general, it is stressed that any non-linear failure criterion $f_{E,I}{}^{i}$ for the constituent materials can be assumed. As experimental evidences show, basic failure modes for masonry walls with weak mortar are a mixing of sliding along the joints (a), direct tensile splitting of the joints (b) and compressive crushing at the interface between mortar and bricks (c). These modes can be gathered adopting a Mohr–Coulomb failure criterion combined with tension cut-off and cap in compression. In addition, for bricks, a classic Mohr–Coulomb failure criterion in plane stress seems to approximate in a reasonable manner block behaviour at failure. Both failure surfaces are schematically represented in Figure 4.

Interfaces failure surfaces are inherently linear and no linearisation routines are needed. Non-linear failure surfaces, however, might be easily dealt with within an LP scheme (abundant literature is available on this topic, see e.g. Milani *et al.*, 2006b): a discussion on the effects of the linearisation of non-linear failure surfaces, however, is beyond the scope of this paper and is, in any case, a classic issue that has been extensively treated in specialised literature.

5. Model III: compatible identification with joints reduced to interfaces and infinitely strong blocks

In this third model, presented by Cecchi *et al.* (2007) for the analysis of Reissner Mindlin homogenised plates, bricks are supposed infinitely resistant, whereas for joints a Mohr–Coulomb failure criterion with tension cut-off and compressive limited strength is adopted (Figure 3(b)). In this way, a full description of the model can be given at a 'micro-scale' considering a representative volume constituted by a generic brick interacting with its six neighbours (Figures 5 and 6). A sub-class of possible elementary deformation modes acting in the unit cell is a priori chosen with the aim of describing joints cracking (Figure 6). Then, a numerical procedure of identification between the three-dimensional (3D) discrete
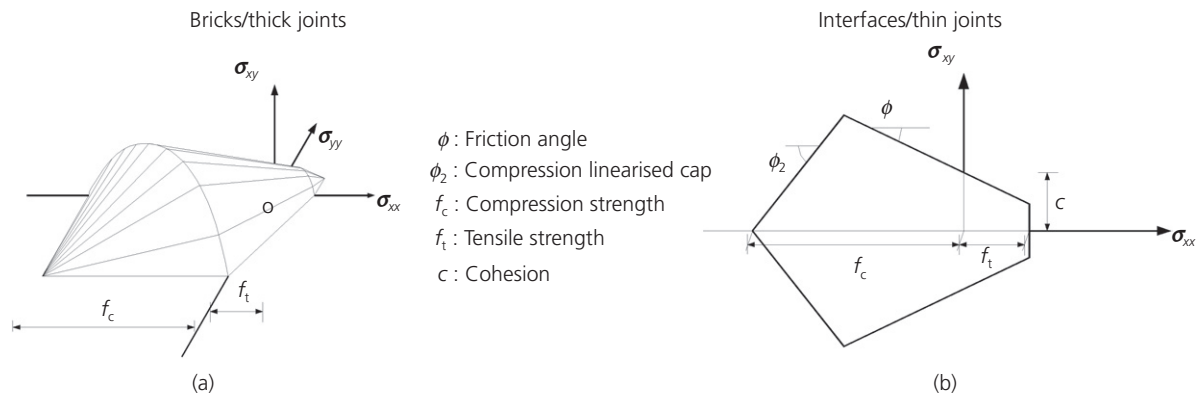
Figure 4. Typical piecewise linear approximation of the failure criteria adopted for bricks and joints: (a) plane stress Mohr–Coulomb failure criterion and (b) Mohr–Coulomb failure criterion with tension cut-off and linearised compression cap
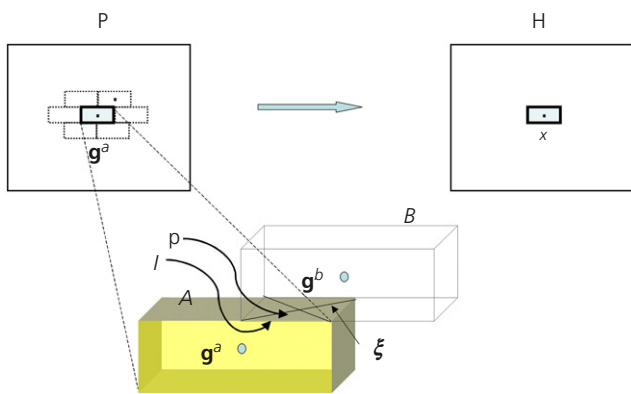

Figure 5. Representative volume element and identification between discrete model and continuous model

system and a continuum 2D equivalent model is proposed, equating internal power dissipation of the two models (Figure 5).

It is interesting to note that the heuristic 'identification approach' here recalled may be regarded as a special application of the general upper bound limit analysis homogenisation problem 4, where joints are reduced to interfaces and bricks are infinitely resistant. When joints obey a classic Mohr–Coulomb failure criterion, problem 4 has been solved in closed form using a rhombic elementary cell by de Buhan and de Felice (1997). In such a case, the homogenised failure surface is constituted by either four or six planes, as schematically illustrated in Figure 7.

Here, a more intuitive and straightforward formulation is provided, that in Cecchi *et al.* (2007) is denoted as 'compatible
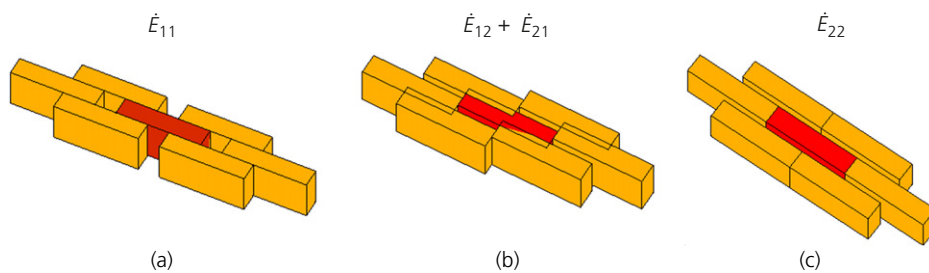
Figure 6. Deformation modes considered in the compatible identification model: (a) horizontal stretching; (b) shear; and (c) vertical stretching
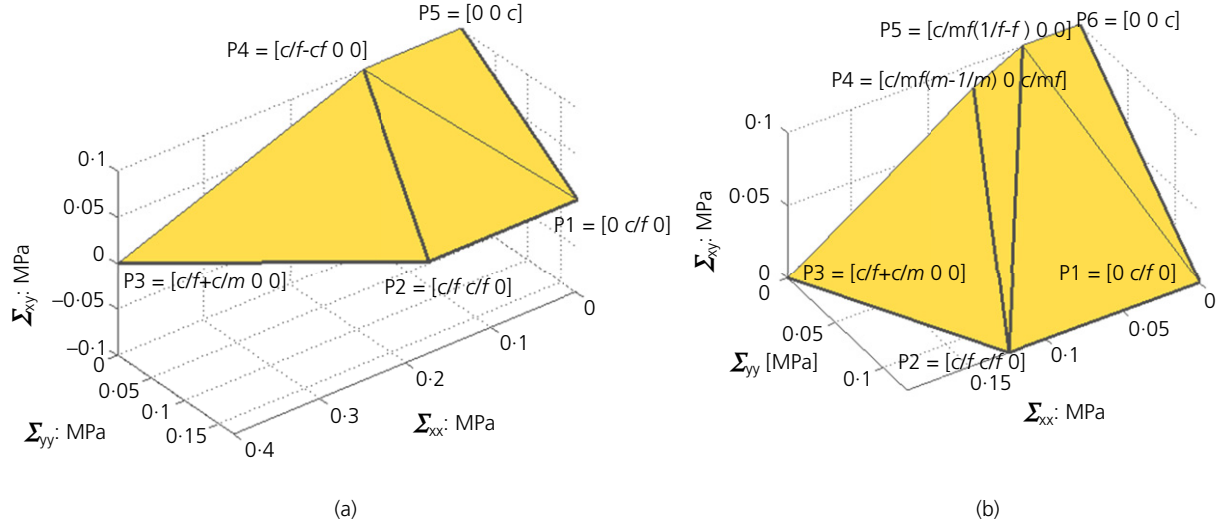
Figure 7. de Buhan and de Felice (1997) failure surface obtained in the presence of infinitely resistant bricks and joints reduced to interfaces with Mohr–Coulomb failure criterion, $m = 2a/b$, $f = \tan\Phi$: (a) $mf \leq 1$ and (b) $mf > 1$

identification'. Let us assume that the motion of a generic brick A is described as a function of its centroid (C^A) velocity $\boldsymbol{v}^{C^A}$ (components $v_{xx}^{C^A}$, $v_{yy}^{C^A}$) and of out-of-plane rotation rate Φ_{zz}^{A}.

When two contiguous bricks A and B are considered, the velocity of a generic point $\boldsymbol{P}$ in a position $\xi \in I$ belonging, respectively, to A and B (where I indicates the common interface between the two bricks) is

12.
$$\boldsymbol{v}^A(\xi) = \boldsymbol{v}^{C^A} + \boldsymbol{M}(\Phi_{zz}^A)(\xi - \mathbf{C}^A)$$
$$\boldsymbol{v}^B(\xi) = \boldsymbol{v}^{C^B} + \boldsymbol{M}(\Phi_{zz}^B)(\xi - \mathbf{C}^B)$$

where $\mathbf{M}(\Phi_{zz}^{A})$ is a standard skew rigid rotation matrix. In Equation 12, the position ξ of point $\boldsymbol{P}$ is evaluated with reference to a local frame of reference (ξ_1 ξ_2) with origin on the centroid on the interface (Figure 5). Jump of velocity $[\boldsymbol{v}(\xi)]$ between bricks A and B in a point $\xi \in I$ is expressed by

13.
$$\lfloor\boldsymbol{v}(\xi)\rfloor = \boldsymbol{v}^B(\xi) - \boldsymbol{v}^A(\xi)$$
$$= \boldsymbol{v}^{C^A} - \boldsymbol{v}^{C^B} + \mathbf{M}(\Phi_{zz}^A)(\xi - \mathbf{C}^A) - \mathbf{M}(\Phi_{zz}^B)$$
$$\times (\xi - \mathbf{C}^B)$$

Power dissipated at the interface I can be written as

14.
$$\pi = \int_I \left[\boldsymbol{t}^A(\xi) \cdot \boldsymbol{v}^A(\xi) + \boldsymbol{t}^B(\xi) \cdot \boldsymbol{v}^B(\xi)\right] \mathrm{d}S$$
$$= \int_I \boldsymbol{t}^A(\xi) \cdot [\boldsymbol{v}(\xi)]\mathrm{d}S$$

where $\boldsymbol{t}^A(\xi) = [\tau_{nt}(\xi)\ \sigma_{nn}(\xi)]^T$ is the stress vector acting at ξ on brick A, $\boldsymbol{t}^A(\xi) = -\boldsymbol{t}^B(\xi)$ and $\tau_{nt}(\sigma_{nn})$ is the tangential (normal) stress acting on the interface.

A standard 2D Cauchy continuum, identified by its middle plane S, is assumed as a 2D homogenised model (Figure 5).

Power dissipated by the equivalent plate model is $\pi = \boldsymbol{ND}$, where $\boldsymbol{D} = \left[\dot{E}_{11}\ \dot{E}_{12} + \dot{E}_{21}\ \dot{E}_{22}\right]^T$ is the in-plane strain rate vector and $\boldsymbol{N} = t[\Sigma_{xx}\Sigma_{xy}\Sigma_{yy}]$ is the vector collecting homogenised internal actions, with t being the thickness of the wall. The application of $\boldsymbol{D}$ vector to the elementary cell corresponds to a univocal deformation mode. Figure 6 shows the effect on the elementary cell of the application of unitary values of $\boldsymbol{D}$ components, stretching along the horizontal axis, shear and vertical axis. It is interesting to note that, when the REV is subjected to horizontal in-plane stretching, both head and bed joints contribute to the ultimate strength, whereas in vertical stretching only in the bed joints a non-null jump of velocities is present.

In the evaluation of the internal power dissipation, it should be noted that, since the jump of velocity on interfaces is assumed to vary linearly in the discrete model, see Equation 13, for each interface $3n_{\text{lin}}$ independent plastic multiplier rates are assumed as optimisation variables.

In this way, for each interface I, the following equality constraints between plastic multiplier rate fields $\dot{\lambda}_i^I(\xi_1, \xi_2)$ and jump of velocity $[w(\xi_1, \xi_2)]$ field on the interface are imposed (associated flow rule)

15.
$$[w(\xi_1, \xi_2)] = \sum_{i=1}^{n_{\text{lin}}} \dot{\lambda}_i^I(\xi_1, \xi_2) \frac{\partial f_I}{\partial \boldsymbol{\sigma}}$$

where $\boldsymbol{\xi} = (\xi_1, \xi_2)$ is a local frame of reference laying on the interface plane and with axis ξ_3 orthogonal to the interface plane; $[w(\xi_1, \xi_2)] = [\Delta w_{\text{nt}} \ \Delta w_{\text{nn}}]^{\text{T}}$ is the jump of velocity field (linear in (ξ_1, ξ_2)) on the Ith interface, with Δw_{nt} and Δw_{nn} being the tangential and normal jumps, respectively; $\dot{\lambda}_i^I(\xi_1, \xi_2)$ is the ith plastic multiplier rate field (linear in (ξ_1, ξ_2)) of the interface I, associated with the ith linearisation plane of the failure surface.

To satisfy Equation 15 for each point of the interface I, nine equality constraints for each interface have to be imposed that corresponds to evaluate 15 in three different positions $P_k = \left(\xi_1^{P_k}, \xi_2^{P_k}\right)$ on the interface I as follows

16.
$$[w(\xi_1^{P_k}, \xi_2^{P_k})] = \sum_{i=1}^{n_{\text{lin}}} \dot{\lambda}_i^I(\xi_1^{P_k}, \xi_2^{P_k}) \frac{\partial f_I}{\partial \boldsymbol{\sigma}}, \quad k = 1, 2, 3$$

where $\dot{\lambda}_i^I\left(\xi_1^{P_k}, \xi_2^{P_k}\right)$ is the ith plastic multiplier rate of the interface I corresponding to $P_k = \left(\xi_1^{P_k}, \xi_2^{P_k}\right)$.

Internal power dissipated on the Ith interface, defined as the product of the interface stress vector for the jump of velocities, is evaluated by means of the following equation

17.
$$\pi_{\text{int}}^I = \int_{A^I} [w]^{\text{T}} \boldsymbol{\sigma} \, dA^I = \int_{A^I} \sum_{i=1}^{n_{\text{lin}}} \dot{\lambda}_i^I(\xi_1, \xi_2) \left[\frac{\partial \varphi}{\partial \boldsymbol{\sigma}}\right]^{\text{T}} \boldsymbol{\sigma} \, dA^I$$
$$= \frac{1}{3} \sum_{i=1}^{n_{\text{lin}}} c_i^I \sum_{k=1}^{3} \dot{\lambda}_i^I\left(\xi_1^{P_k}, \xi_2^{P_k}\right) A^I$$

External power dissipated can be written as $\pi_{\text{ext}} = (\boldsymbol{\Sigma}_0^{\text{T}} + \Lambda \boldsymbol{\Sigma}_1^{\text{T}})\boldsymbol{D}$, where $\boldsymbol{\Sigma}_0$ is the vector of permanent loads, Λ is the load multiplier and $\boldsymbol{\Sigma}_1^{\text{T}}$ is the vector of loads dependent on the load multiplier (i.e. the optimisation direction in the space of macroscopic stresses). As the amplitude of the failure mechanism is arbitrary, a further normalisation condition $\boldsymbol{\Sigma}_1^{\text{T}}\boldsymbol{D} = 1$ is

usually introduced. Hence, the external power becomes linear in $\boldsymbol{D}$ and Λ and can be written as $\pi_{\text{ext}} = \boldsymbol{\Sigma}_0^{\text{T}}\boldsymbol{D} + \Lambda$.

From previous considerations, it is quite straightforward to conclude that a linear relation between $\boldsymbol{D}$ and $[w(\xi_1, \xi_2)]$ may be written for each interface I as follows

18.
$$[w(\xi_1, \xi_2)] = \boldsymbol{G}^I(\xi_1, \xi_2)\boldsymbol{D}$$

where $\boldsymbol{G}^I(\xi_1, \xi_2)$ is a 3×10 matrix that depends only on the geometry of the interface under consideration.

Making use of both Equations 15–18 and of the kinematic formulation of limit analysis, the following constrained minimisation problem is finally obtained to estimate the load multiplier Λ (having the same meaning of the previous lower bound models)

19.
$$\begin{cases} \Lambda = \min_{\hat{\boldsymbol{x}} = [\boldsymbol{D}, \dot{\lambda}_i^I(P_k)]} \sum_{I=1}^{n^I} \pi_{\text{int}}^I - \boldsymbol{\Sigma}_0^{\text{T}}\boldsymbol{D} \\ \boldsymbol{\Sigma}_1^{\text{T}}\boldsymbol{D} = 1 \\ \boldsymbol{G}^I(P_k)\boldsymbol{D} = [w(P_k)] = \sum_{i=1}^{n_{\text{lin}}} \dot{\lambda}_i^I\left(\xi_1^{P_k}, \xi_2^{P_k}\right) \frac{\partial \varphi}{\partial \boldsymbol{\sigma}}, \quad P_k \in I \end{cases}$$

where n^I is the total number of interfaces considered and $\hat{\boldsymbol{x}}$ is the vector of total optimisation unknowns. Vector $\hat{\boldsymbol{x}}$ of global unknowns collects only $3n_{\text{lin}}n^I$ plastic multiplier rates and macroscopic kinematic variable $\boldsymbol{D}$.

Problem 19 leads to reproduce the macroscopic in-plane failure surface of masonry through a kinematic approach.

6. Model IV: upper bound MoC with actual joint thickness

The so-called MoC was originally proposed by Aboudi (1991) for unidirectional composites reinforced by a regular pattern of long, reinforcing fibres. MoC has been recently extended to masonry by Taliercio (2014) for the macroscopic elastic and creep coefficients determination in closed form and by Milani and Taliercio (2015) in the limit analysis case. The method, applied to running bond masonry in-plane loaded, consists of the subdivision of the REV into six rectangular sub-cells, as shown in Figure 8, where the velocity field is approximated using two sets of strain-rate periodic piecewise differentiable velocity fields, one for normal and one for shear deformation mode.

Let us indicate with symbols $\boldsymbol{u}_1^{(i)}$ and $\boldsymbol{u}_2^{(i)}$, vertical and horizontal velocity fields of the ith cell for the deformation mode acting axially along vertical and horizontal directions. Assuming the same periodic field proposed for displacements in the elastic range by Taliercio (2014), the following

relations hold

$$u_1^{(2)} = 2U_1\frac{x_1}{b_b}, \quad u_2^{(1)} = -2W_1\frac{x_2}{h_b}$$

$$u_1^{(2)} = U_1 + \frac{(U_2 - U_1)\left(x_1 - \dfrac{b_b}{2}\right)}{b_m}, \qquad u_2^{(2)} = -2\frac{x_2}{h_b}\left(\frac{2(W_1 - W_2)\left|\dfrac{b_m + b_b}{2} - x_1\right|}{b_m} + W_2\right)$$

$$u_1^{(3)} = u_1^{(1)} - \frac{(U_1(1 + 2\alpha_b) - U_2)\left(\dfrac{h_b}{2} - x_2\right)}{2h_m}, \quad u_2^{(3)} = -W_1 + \frac{(W_1 - W_3)\left(x_2 - \dfrac{h_b}{2}\right)}{h_m}$$

$$u_1^{(4)} = u_1^{(1)} + \frac{(U_1(1 + 2\alpha_b) - U_2)\left(\dfrac{h_b}{2} - x_2\right)}{2h_m}, \quad u_2^{(4)} = u_2^{(3)}$$

20.

$$u_1^{(5)} = U_1 - \frac{(U_1(1 + 2\alpha_b) - U_2)\left(\dfrac{b_b + b_m}{2} - x_1\right)\left(x_2 - \dfrac{h_b}{2}\right)}{b_m h_m} - \frac{(U_1 - U_2)\left(x_1 - \dfrac{b_b}{2}\right)}{b_m}$$

$$u_2^{(5)} = -W_3\frac{x_2 - \dfrac{h_b}{2}}{h_m} - 2\frac{\left(W_2\dfrac{b_m}{2} - (W_2 - W_1)\left|\dfrac{b_b + b_m}{2} - x_1\right|\right)\left(\dfrac{h_b}{2} + h_m - x_2\right)}{b_m h_m}$$

$$u_1^{(6)} = 2\frac{x_1}{b_b}\left(U_1 - \frac{\left(U_1 + \dfrac{U_1 - U_2}{2\alpha_b}\right)\left(x_2 - \dfrac{h_b}{2}\right)}{h_m}\right)$$

$$u_2^{(6)} = -W_1 + \frac{\left(W_2 - W_3 + 2(W_1 - W_2)\dfrac{|x_1|}{b_m}\right)\left(x_2 - \dfrac{h_b}{2}\right)}{h_m}$$

An additional constraint $W_1 = W_2$ is imposed in the model in order to avoid bilinear terms of the velocity field in cross-

When a shear deformation mode is applied on the REV, the following fields of velocity are assumed to be inside each cell

$$u_1^{t(1)} = 2U_1^t\frac{x_2}{h_b}, \quad u_2^{t(1)} = 0, \quad u_1^{t(2)} = u_1^{t(1)}, \quad u_2^{t(2)} = W_1^t\frac{x_1 - (b_b/2)}{b_m}$$

$$u_1^{t(3)} = U_1^t + \frac{U_2^t - U_1^t}{h_m}\left(x_3 - \frac{h_b}{2}\right), \quad u_2^{t(3)} = -W_2^t\frac{x_2 - (b_b/2)}{h_m}$$

21. $$u_1^{t(4)} = u_1^{t(3)}, \quad u_2^{t(4)} = -u_2^{t(3)}$$

$$u_1^{t(5)} = u_1^{t(3)}, \quad u_2^{t(5)} = -W_1^t\frac{(x_1 - (b_b + b_m/2))(x_2 - (h_b/2)) - h_m(x_1 - (b_b/2))}{b_m h_m}$$

$$u_1^{t(6)} = u_1^{t(3)}, \quad u_2^{t(6)} = W_1^t\frac{x_1(x_2 - (h_b/2))}{b_m h_m}$$

joints. Bilinearity makes the check of the associated flow rule inside cross-joints cumbersome, with an experienced negligible modification of the final result.

Fields 20 depend on U_1, U_2, W_1, $W_2 = W_1$ and W_2 degree of freedom (DOF) velocities, with clear physical meaning represented in Figure 9. Frame of reference x_1–x_2 and geometrical meaning of the symbols are provided in Figure 8. α_b is the ratio between b_m and b_b, respectively, bed joint thickness and brick length. It is interesting to note that the velocity fields inside each cell are either linear (cells 1, 3, 4) or quadratic (cells 2, 5, 6).

Symbols $u_1^{t(i)}$ and $u_2^{t(i)}$ in Equation 21 indicate vertical and horizontal velocity fields of the ith cell for the shear deformation mode imposed. In Equation 21, independent variables (DOFs) are represented by U_1^t, U_2^t, W_1^t and W_2^t. An additional constraint $W_1^t = 2W_2^t$ is imposed in the model to make the velocity field compatible between cross-joints and contiguous sub-cells. The physical meaning of the unknown shear velocity parameters is depicted in Figure 10.

According to the kinematic theorem of limit analysis, Equation 4 and assuming the velocity field over the REV to be
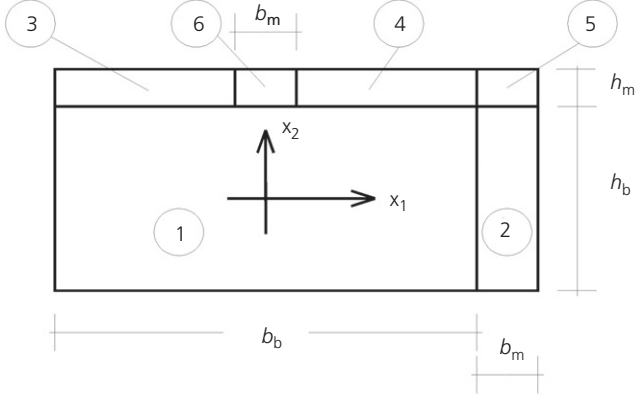
Figure 8. REV adopted in the MoC approach and subdivision into cells

approximated by means of the expressions provided by Equations 20 and 21, the associativity of the plastic flow over each sub-cell must be prescribed.

Let $v_1 = v_1^{n(i)} + v_1^{t(i)}$ and $v_2 = v_2^{n(i)} + v_2^{t(i)}$ denote the horizontal and vertical components of the velocity field in the (i)th sub-cell. At each point of any sub-cell, the associated flow rule

translates into three equality constrains, which can be written as $\dot{\varepsilon}_{pl}^{(i)} = [(\partial v_1/\partial y_1)\,(\partial v_2/\partial y_2)\,(\partial v_1/\partial y_2) + (\partial v_2/\partial y_1)] = \dot{\lambda}^{(i)}(\partial f_{b,m}/\partial \sigma)$, where $\dot{\varepsilon}_{pl}^{(i)}$ is the plastic strain rate field in the (i)th sub-cell; $\dot{\lambda}^{(i)}$ (≥ 0) is the rate of the plastic multiplier, and $f^{b,m}$ is the (non)-linear failure surface of either bricks (b) or mortar (m). Let the failure surfaces of bricks and mortar be approximated by m planes (see Figure 4), so that each strength criterion is defined by a set of linear inequalities of the form $f_{b,m} \equiv \mathbf{A}^{in}\sigma \leq \mathbf{b}^{in}$. As $\dot{\varepsilon}_{pl}^{(i)}$ varies at most linearly within each sub-cell, plastic admissibility is checked only at three of the corners. Hence, nine linear equality constraints per sub-cell are introduced in the matrix form as $A_{U(i)}^{eq}U + A_{\lambda(i)}^{eq}\dot{\lambda}^{(i)} = \mathbf{0}$, where U is an array collecting the seven DOFs describing the microscopic velocity field (i.e. $U = \{U_1,\,U_2,\,W_1,\,W_2,\,U_1^t,\,U_2^t W_1^t\}^T$); $\dot{\lambda}^{(i)} = \left[\dot{\lambda}_A^{(i)T}\,\dot{\lambda}_B^{(i)T}\,\dot{\lambda}_C^{(i)T}\right]^T$ is an array of $3m$ entries, collecting the rates of the plastic multipliers $\dot{\lambda}_J^{(i)}$ at three of the corners of the rectangular sub-cell (J = A, B, C); and $\mathbf{A}_{U(i)}^{eq}$, $\mathbf{A}_{\lambda(i)}^{eq}$ are 9×7 and a $9 \times 3m$ matrices, respectively. The plastic admissibility conditions are then assembled cell by cell into the following global system of equality constraints

22. $A_U^{eq}U + A_\lambda^{eq}\dot{\lambda} = \mathbf{0}$

where $\mathbf{A}_U^{eq} = \left[A_{U(1)}^{eq}\mathrm{T}\,\cdots\,A_{U(6)}^{eq}\mathrm{T}\right]^T$, $\dot{\lambda} = \left[\dot{\lambda}^{(1)}\mathrm{T}\,\cdots\,\dot{\lambda}^{(6)}\mathrm{T}\right]^T$ and $\mathbf{A}_\lambda^{eq}$ is a block matrix of dimension $(6 \times 9) \times (6 \times 3m)$,
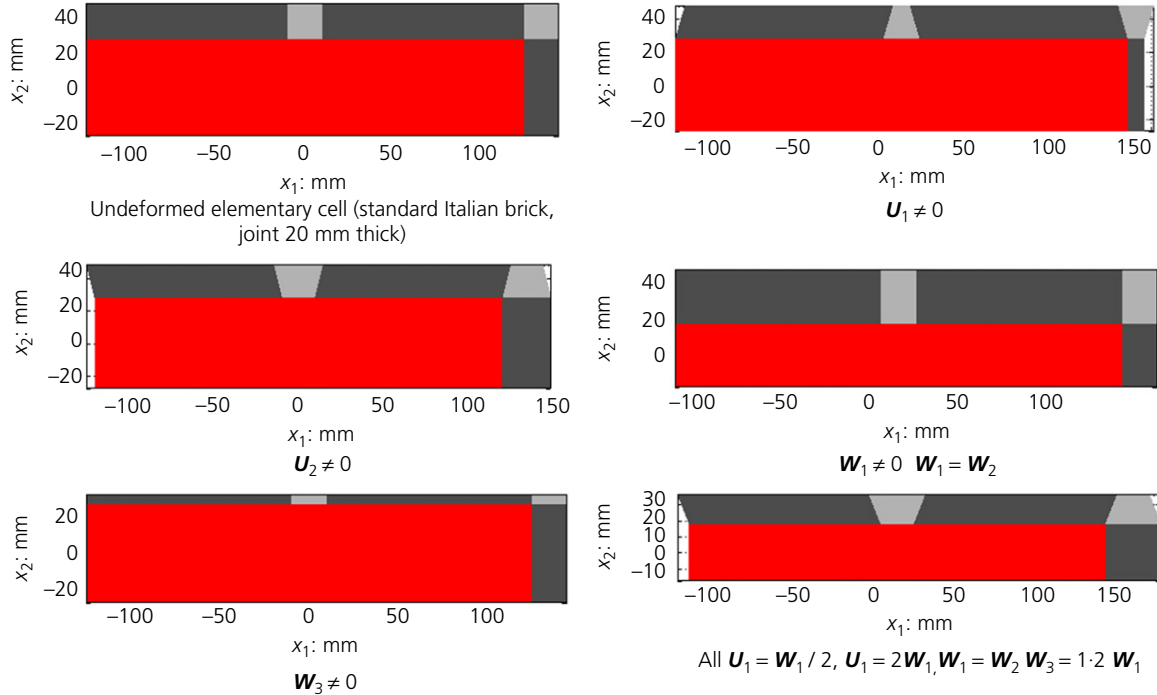

Figure 9. Strain rate periodic kinematically admissible velocity field under horizontal or vertical macroscopic stresses
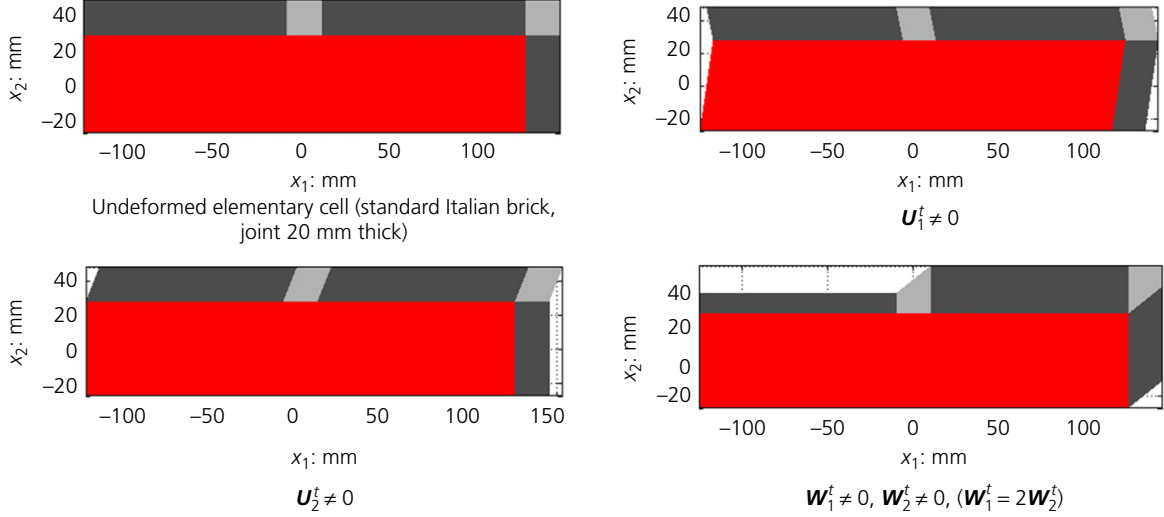
Figure 10. Strain rate periodic kinematically admissible velocity field under shear

which can be expressed as

23.
$$\mathbf{A}_\lambda^{eq} = \mathbf{A}_{\lambda(1)}^{eq} \oplus \mathbf{A}_{\lambda(2)}^{eq} \oplus \cdots \oplus \mathbf{A}_{\lambda(6)}^{eq}$$

where $\oplus$ denotes direct sum.

Let B and C be a couple of corners at the opposite ends of one of the diagonals of the (i)th rectangular sub-cell. The internal power dissipated within the sub-cell can be written as

24.
$$\begin{aligned}
\pi_{in}^{(i)} &= \frac{\Omega^{(i)}}{2} \left(\mathbf{b}_{in}^{(i)T} \dot{\lambda}_B^{(i)} + \mathbf{b}_{in}^{(i)T} \dot{\lambda}_C^{(i)} \right) \\
&= \frac{\Omega^{(i)}}{2} \begin{bmatrix} \mathbf{0}_{1 \times m} & \mathbf{b}_{in}^{(i)T} & \mathbf{b}_{in}^{(i)T} \end{bmatrix} \dot{\lambda}^{(i)}
\end{aligned}$$

where $\mathbf{0}_{1 \times m}$ is an array of m zero entries and $\Omega^{(i)}$ is the area of the (i)th sub-cell. The power dissipated inside the whole RVE is obviously the sum of the contributions of each sub-cell, that is

25.
$$\pi_{in} = \sum_{i=1}^{6} \frac{\Omega^{(i)}}{2} \begin{bmatrix} \mathbf{0}_{1 \times m} & \mathbf{b}_{in}^{(i)T} & \mathbf{b}_{in}^{(i)T} \end{bmatrix} \dot{\lambda}^{(i)}$$

The array of the macroscopic stress components can be expressed as $\Sigma = \Lambda[\alpha\ \beta\ \gamma]^T$, where Λ is the load multiplier and α, β, γ are the already defined director cosines of the Σ direction.

The power of the external loads is simply $\pi_{ex} = \Lambda[\alpha\ \beta\ \gamma]\boldsymbol{D}$ with the normalisation condition given by $[\alpha\ \beta\ \gamma]\boldsymbol{D} = 1$.

Similarly to model III, any point of the homogenised failure surface is thus determined solving the following constrained

minimisation problem

26.
$$\min \pi_{in}$$
$$\text{s.t.} \begin{cases} \begin{cases} [\alpha\ \beta\ \gamma]\boldsymbol{D} = 1 & \text{(a)} \\ \mathbf{A}_U^{eq}\boldsymbol{U} + \mathbf{A}_\lambda^{eq}\dot{\lambda} = \mathbf{0} & \text{(b)} \\ \boldsymbol{D} = \frac{1}{A}\int_{\partial Y} \boldsymbol{v} \overset{s}{\otimes} \boldsymbol{n}\, \mathrm{d}S & \text{(c)} \\ \dot{\lambda} \geq \mathbf{0} & \text{(d)} \end{cases} \end{cases}$$

where (a) is the normalisation condition, (b) is the set of equations representing the admissibility of the plastic flow, Equation 22, and (c) links the homogenised strain rate with the local velocity field.

It is interesting to note that the independent variables entering into the optimisation problem 26 are the three components of the macroscopic strain rate $\boldsymbol{D}$, the $6 \times 3m$ plastic multipliers $\dot{\lambda}$ and the seven DOFs defining the microscopic velocity field. By way of the normalisation condition and equating the internal power dissipation to the power of the external loads, it can be easily shown that $\Lambda = \min \pi_{in}$.

7. Comparison on real case studies

Some case studies are considered in this section, in order to evaluate the capabilities and the limitations of the four limit analysis homogenisation strategies reviewed in the paper. Some considerations on the numerical efficiency of the models presented are also briefly recalled.

7.1 Failure surfaces in the tension–tension and compression–compression regions

The first numerical simulations are referred to a running bond masonry constituted by standard Italian bricks (dimensions $250 \times 120 \times 55 \text{ mm}^3$) and joints of 10 mm thickness.

Mechanical properties adopted for mortar are summarised in Table 1, whereas bricks are assumed as infinitely resistant. It is interesting to note that when the actual thickness of the joints is considered in the computations, – that is for the first and fourth models, a limited tensile and compressive strength is assumed for mortar, automatically defined for plane stress conditions with relations reported in Table 1. When dealing with interface models (i.e. first and third models), an infinite compression strength is assumed, whereas for tensile strength f_t a cut-off equal to that assumed for thick joint is adopted.

As already pointed out, an explicit homogenised strength domain in the case of infinitely resistant units and joints reduced to interfaces has been derived by de Buhan and de Felice (1997). The reduction of joints to interfaces with a Mohr–Coulomb failure criterion combined with the infinite resistance of units makes possible to find, through a kinematic approach, an explicit solution for the homogenisation problem in the rigid-plastic case. It can be shown that the homogenised material so derived is infinitely resistant in the compression–compression region, while is orthotropic at failure in the tension–tension field (Figure 7).

The convergence of the polynomial expansion to the actual solution has been demonstrated in Milani *et al.* (2006a), where the reader is referred for further details, and occurs obviously with a lower bound approximation, as shown in Figure 11, where a comparison with finite-element method (FEM) solution is provided in the tension–tension region assuming that the bed joint direction is parallel to one of the principal load directions.

As can be noted, both P3 and P4 models well approximate FEM, whereas for P0 orthotropy at failure is completely lost. Results for P1 are not reported because, due to the boundary conditions to be imposed on the REV, they coincide with P0.

In Figure 12, a comparison among failure surfaces obtained using the four discussed models is presented in the tension–tension region and for the masonry material of Table 1. In particular, Figure 12(a) refers to $\vartheta = 45°$, Figure 12(b) refers to $\vartheta = 22.5°$ and Figure 12(c) refers to $\vartheta = 0°$. CST equilibrated approach (model II) and compatible identification (model III) provide the same results. Since the first is a lower bound approach and the latter an upper bound approximation, theorems of classic limit analysis secure that the approximations

Frictional angle (Φ)	Cohesion (c)
36°	0·1 MPa
$f_t = \dfrac{2c\cos(\Phi)}{1 + \sin(\Phi)}$	$f_c = \dfrac{2c\cos(\Phi)}{1 - \sin(\Phi)}$

Table 1. Mechanical properties adopted in the first set of numerical simulations
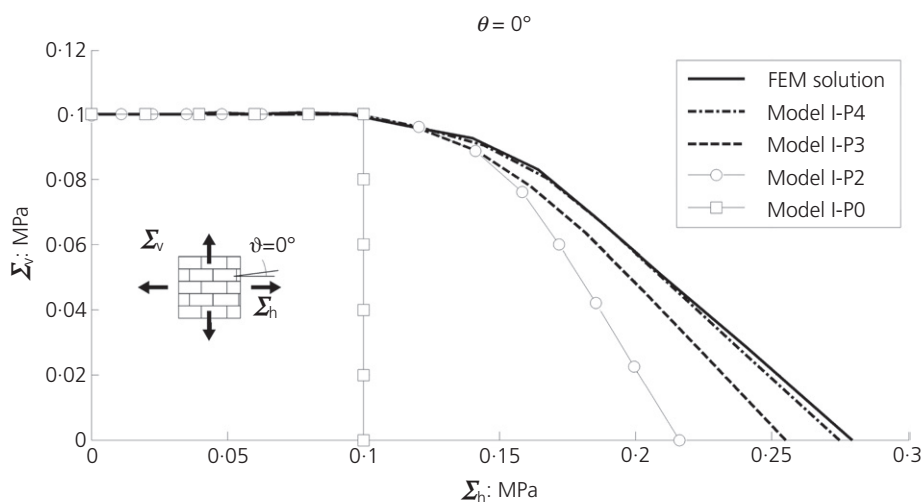

Figure 11. Convergence of the different polynomial expansion models for the masonry material of Table 1 and the direction of the principal axes parallel to that of material axes ($\vartheta = 0°$)
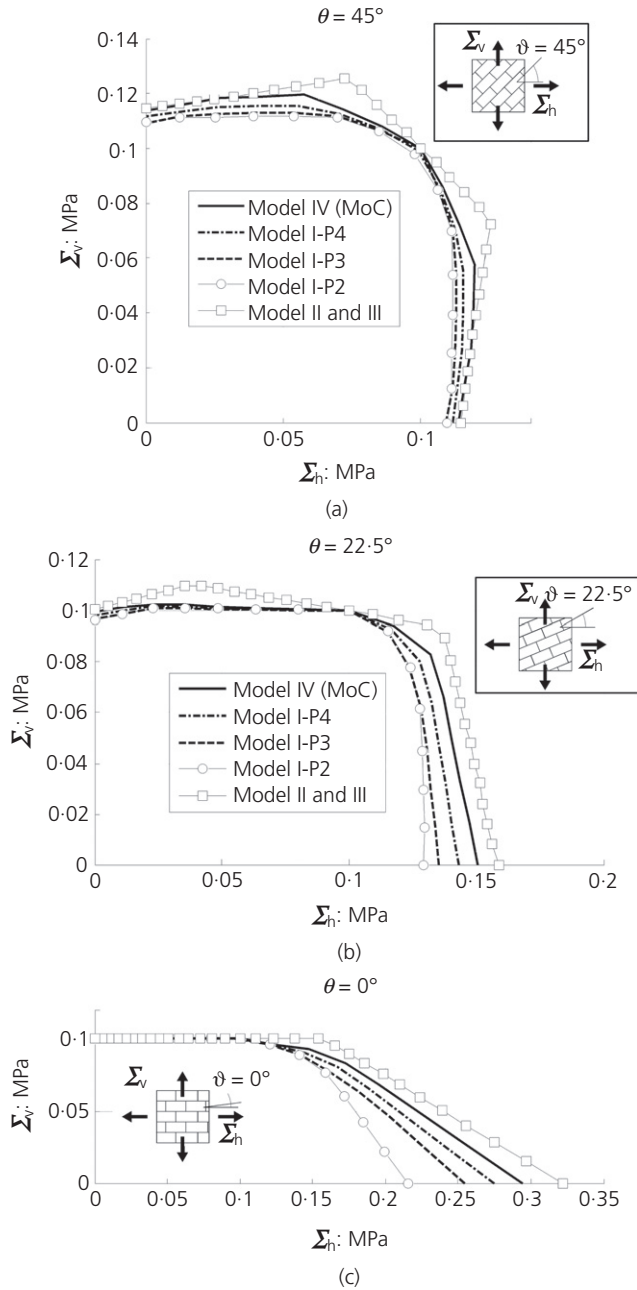
Figure 12. Comparison among the different homogenisation models proposed in the tension–tension region for the masonry material of Table 1: (a) $\vartheta = 45°$; (b) $\vartheta = 22.5°$; and (c) $\vartheta = 0°$

represent the actual homogenised failure surface in case of joints reduced to interfaces.

The dependence of the homogenised failure surfaces from joint thickness is worth noting, looking into the results reported in Figure 12 (compare, for instance, results obtained with MoC

or P4 with model II output). The presence of thick joints is linked to the evaluation of a smoother failure surface, which reduces to the multi-plane strength domain in the case of joints reduced to interfaces, as shown by de Buhan and de Felice (1997).

Maximum horizontal strength is obtained for $\vartheta = 0°$, but results lower in the case of thick joints (0.28 against 0.33 MPa, with a percentage difference equal to around 15%).

It is worth mentioning that when the joint thickness is reduced to interface in both models I and IV, a perfect agreement with compatible identification (or CST equilibrated model) is experienced.

Another interesting remark deduced from results reported in Figure 12 is that models I and IV closely bracket the actual homogenised failure surface in the case of finite thickness of joints. The maximum percentage difference between P4 and MoC collapse loads is indeed experienced in pure horizontal stretching (Figure 12(c)), with a difference not exceeding 7%. Considering that model I-P4 is a lower bound, whereas model IV-MoC is an upper bound, the actual failure surface lays somewhere between the aforementioned predictions, with expected errors of lower than 5%, a result fully satisfactory from an engineering standpoint.

It is finally worth mentioning that to obtain the failure surface sections depicted in Figure 12, an extremely reduced computational cost is needed on standard PCs, as shown in Table 2, where processing times are reported, especially in comparison with classic incremental elasto-plastic FEM. Table 2 demonstrates the advantage of using 'direct methods' in the evaluation of the ultimate behaviour of masonry instead of

	Optimisation time min:s
Model I: polynomial expansion	
Degree 0	00:12
Degree 2	01:28
Degree 3	06:33
Degree 4	09:33
Model II: equilibrated triangular coarse mesh	01:44
Model III: kinematic model with rigid blocks and interfaces	01:33
Model IV: MoC	02:19

Table 2. Computational time needed for the estimation of the failure surface sections in Figure 12 (standard 64 bit PC with Win7 OS, 8 GB RAM, SeDuMi LP package solver)

conventional incremental approaches. In addition, it should be remembered that all models presented are much more efficient than a classic discretisation of the unit cell with limit analysis FEs, due to the extremely reduced number of optimisation variables involved.

In Figure 13, the REV deformed shape at collapse for MoC is also represented in the case of $\vartheta = 0°$ and $\psi = 0°$.

As can be noted (and consistently with all other homogenisation models previously presented), the head joint is subjected to pure tensile strength, whereas bed joints to pure shear. Cross-joints, conversely, exhibit a mixed mode failure, which, however, does not influence much the ultimate homogenised strength, due to their negligible area, especially for thin joints.

For the same example of Table 1, the comparison done in the tension–tension region is repeated in the compression–compression region and the results are reported in Figure 14. Results are normalised against mortar joint f_c compression strength. Again the agreement between P4 and MoC models appears rather satisfactory, with negligible differences from an engineering viewpoint.

It is worth noting here that vertical masonry compression strength coincides with mortar compression resistance. Indeed, in all models it is assumed that mortar and bricks undergo plane-stress conditions. As well known, such assumption has strong limitations, especially for the prediction of the ultimate compressive strength of masonry pillars. As a matter of fact, when a plane-stress approach is used, it has been shown by different authors (see, for instance, Addessi and Sacco, 2014; Milani *et al.*, 2006a; Sahlaoui *et al.*, 2011; Stefanou *et al.*, 2014) that the vertical compression strength of masonry is always equal to mortar joint compression resistance, whereas the exact formulation of the unit cell problem is neither reducible to a plane strain nor to a plane stress, but is a truly 3D one (Sahlaoui *et al.*, 2011; Stefanou *et al.*, 2014).

To capture the real behaviour in the compression–compression region, a full 3D approach would be therefore required, namely either by means of an enrichment of the velocity field along the direction perpendicular to the middle plane when an upper bound approach is adopted or with the utilisation of full 3D stress fields in the lower bound case. A work in progress by the author is the extension of MoC to the full 3D case. Such generalisation requires also the utilisation of conic
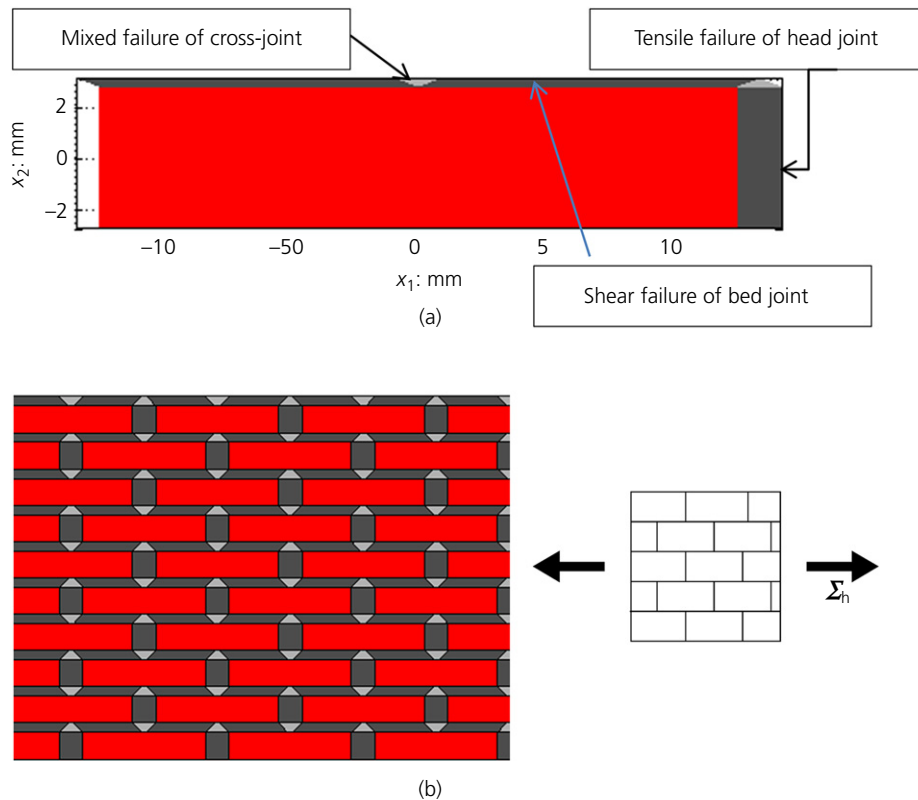

Figure 13. MoC deformed shape for horizontal stretching (single cell (a) and repetition of several unit cells (b))
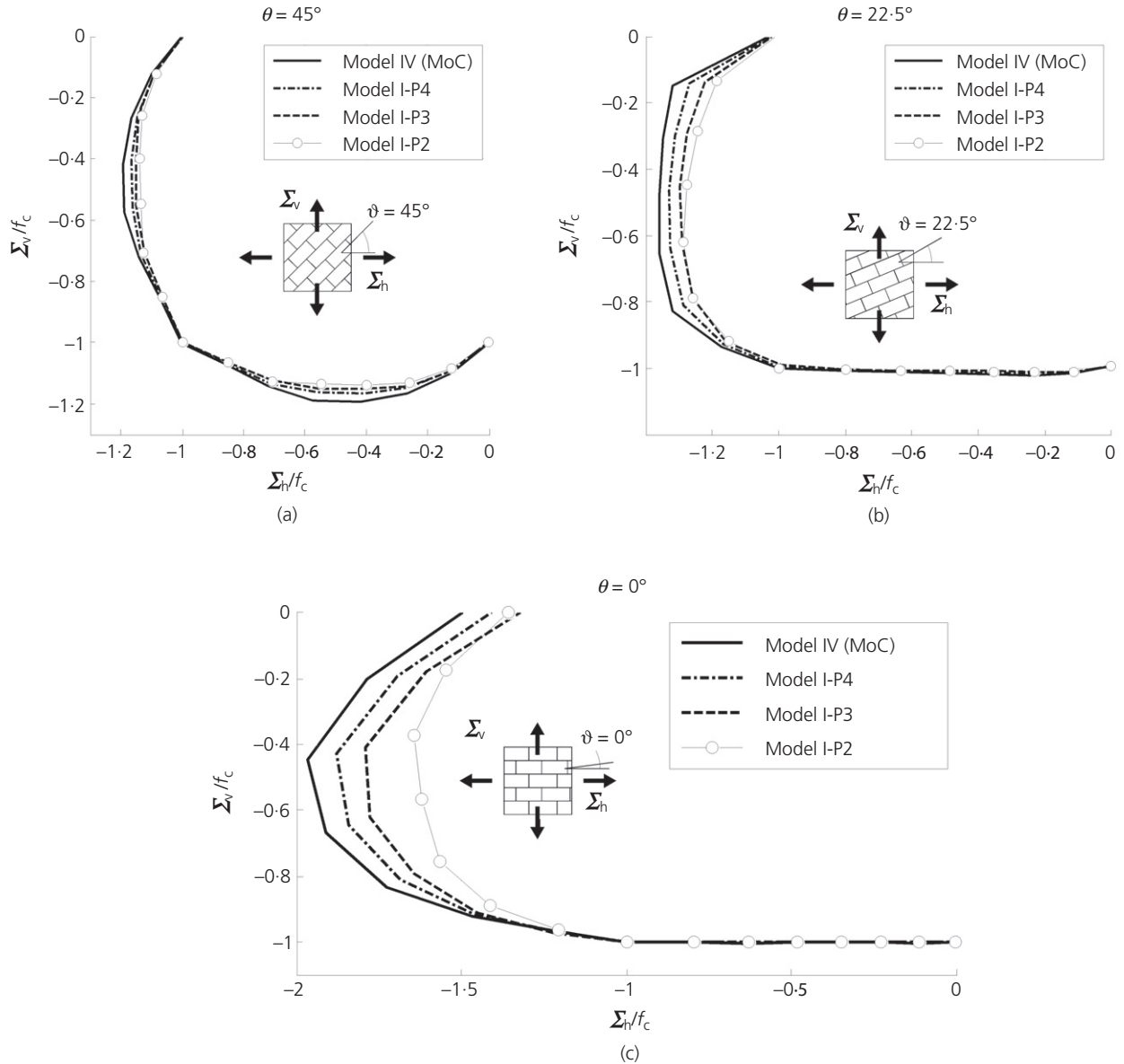
Figure 14. Comparison between polynomial lower bound approximation and MoC in the compression–compression region, mechanical properties of Table 1: (a) $\vartheta = 45°$; (b) $\vartheta = 22·5°$; and (c) $\vartheta = 0°$

programming (Portioli *et al.*, 2014) instead of classic LP to evaluate collapse multipliers.

7.2 Failure surfaces assuming complex strength domains for joints

The last numerical example is devoted to the analysis of a masonry wall, again built with standard Italian bricks disposed in running bond and joints considered either reduced to interfaces or with a thickness equal to 10 mm.

Two different failure surfaces are critically investigated both for thick and thin joints, as shown in Figure 15.

Figure 15(a) shows the two plane stress multi-surface failure criteria used for thick joints. Dashed lines in Figure 15(a) represent sections of the failure surface along the plane $\Sigma_{xx} = \Sigma_{yy}$). The first failure criterion is obtained as the convex envelope of a Mohr–Coulomb failure criterion in plane strain (characterised by parameters c and Φ) and a Rankine failure criterion in

(a)

Multi-linear compression cap

Compression cut-off Rankine failure criterion

Mohr–Coulomb failure criterion in plane strain

c Φ

Tension cut-off Rankine failure criterion

f_c

Σ_{xy}: MPa

1

0·5

0

Tresca strength c_u

f_t

−4

−3

−2

−1

0

Σ_{xx}: MPa

−1

0

−4

−3

−2

−1

Σ_{yy}: MPa

+45° bisecting line principal stress plane

Failure surface 1

Failure surface 2

Σ_{xy}: MPa

1

0·5

0

ρ

$\beta\rho$

0

−2

−4

Σ_{xx}: MPa

0

−1

−2

−3

−4

Σ_{yy}: MPa

Thick joint plane stress failure criterion

Point of intersection between Mohr–Coulomb failure criterion and Rankine failure in compression

Σ_{nt}

Σ_{nn}

Σ_{nt}

Σ_{nn}

Σ_{nn}: MPa

Φ

f_t

c

c_u

Φ_2

f_c

Σ_{nt}: MPa

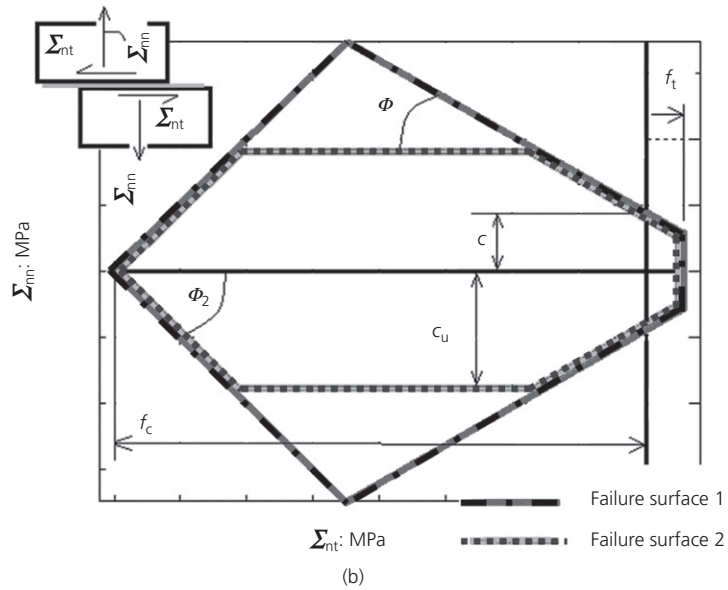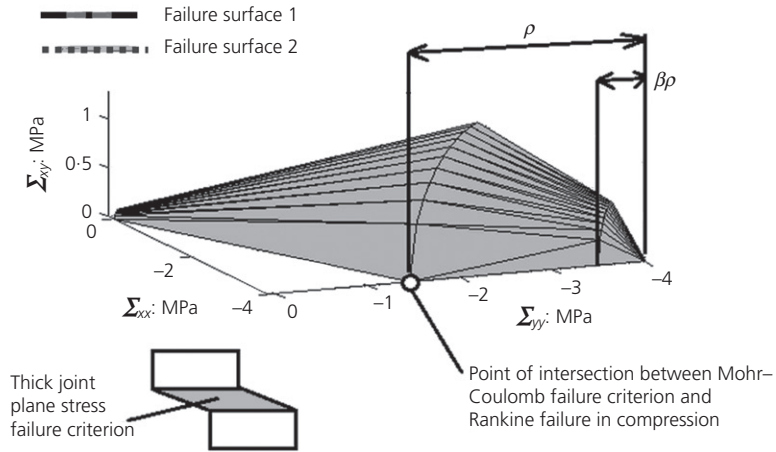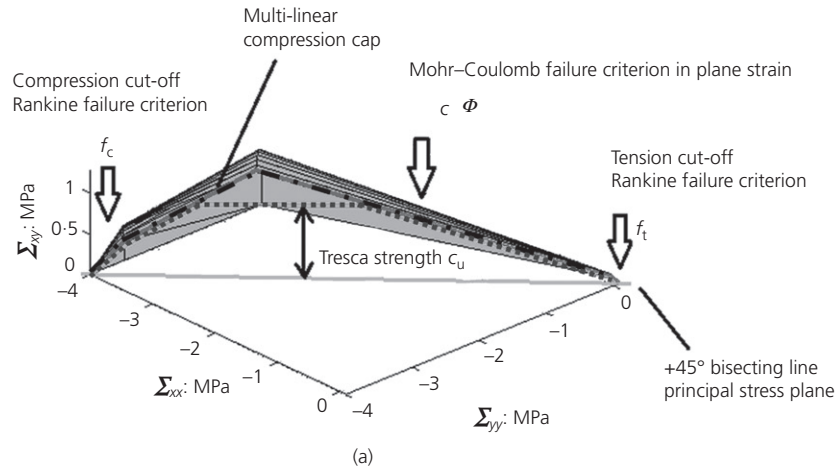Failure surface 1

Failure surface 2

(b)

Figure 15. (a) Plane stress failure criteria adopted for thick mortar joints and (b) interface failure criteria adopted for joints reduced to interfaces

tension and compression (characterised by parameters f_t and f_c). The intersection in the compression region between the Mohr–Coulomb failure criterion and the Rankine failure criterion is obtained with a linear cap, fully defined by the non-dimensional parameter β, with the meaning of the symbol clearly explained in Figure 15(a). The second failure surface is identical, exception made for a cut of the previous surface obtained with a Tresca failure surface in plane strain, univocally determined by the parameter c_u.

When dealing with joints reduced to interfaces, reference is made to the multi-linear failure surfaces depicted in Figure 15 (b) and characterised by a pure Mohr–Coulomb failure criterion, with cap in compression (identified by mechanical parameters Φ_2 and f_c, defining, respectively, the shape of the compression cap and the uniaxial compressive strength), tension cut-off (value of the tensile strength equal to f_t) and eventually (second failure surface) superimposed with a Tresca failure criterion with ultimate cohesion equal to c_u.

The aim of the comparison is to show how the choice of the failure surface may be paramount for an accurate determination of the homogenised ultimate behaviour, especially in the presence of tangential stresses.

A comparison with two well-known macroscopic orthotropic failure criteria, the first proposed by Lourenço (1996) and Lourenço *et al.* (1997) and the second by Berto *et al.* (2002), is also reported, in order to show that macroscopic orthotropic failure criteria are not always predictive of the actual ultimate strength under different loading conditions. A non-negligible effect on the failure surface is also expected reducing joints to interfaces, which reflects in a less smooth shape of the resultant

strength domain, as also observed experimentally (Casapulla and Portioli, 2015; Vasconcelos and Lourenço, 2009).

Mechanical properties adopted for both the homogenisation and the macroscopic models are summarised in Table 3.

Three sections of the homogenised failure surface are investigated, and correspond to lines 1, 2 and 3 in Figure 16(a). Line 1 is the failure surface section with $\Sigma_{yy} = 0$, line 2 corresponds to the constraint $\Sigma_{xx} = 0$, whereas for line 3 $\Sigma_{xx} = \Sigma_{yy}$.

The resulting failure surface sections are depicted in Figure 16 (b) (line 1), Figure 16(c) (line 2) and Figure 16(d) (line 3). The corresponding failure modes obtained in the presence of thick joints are depicted in Figure 17 for some meaningful points of the obtained failure surface, as for instance in horizontal stretching (point A) or pure shear (point B). As in the previous case, the behaviour in compression is again driven by the limited joint strength, an outcome not fully in agreement with experimental evidences (see point F in Figure 17), for the reasons discussed in the previous sub-section. However, as already pointed out, this is an intrinsic limitation of 2D models that cannot be avoided.

In the case of thin joints, failure surfaces presented are obtained with models II and III (but very similar results are obtained using models I and IV when joints are reduced to interfaces), whereas for thick joints obviously only models I and IV are adopted. In all cases, in model I a fourth-order expansion of the micro-stress field is used. The author experienced very little differences on the computed failure surfaces using the different models. Hence, only two homogenised curves are reported for the sake of clearness, one for thin and

Thick joints						
f_c: MPa	f_t: MPa	c: MPa	Φ: deg	c_u: MPa		
4·0	0·1	1·2 f_t	30	2·5c		
Thin joints						
f_c: MPa	f_t: MPa	c: MPa	Φ: deg	Φ_2: deg	c_u: MPa	
4·0	0·1	1·2 f_t	30	45	2·5c	
Orthotropic macroscopic model by Lourenço (1996)						
f_{cxx}: MPa	f_{cyy}: MPa	f_{txx}: MPa	f_{tyy}: MPa	f_{c45}: MPa	c_u: MPa	
4·5	4·0	0·5	0·2	4·5	0·2	
Orthotropic macroscopic model by Berto *et al.* (2002)						
f_{cxx}: MPa	f_{cyy}: MPa	f_{txx}: MPa	f_{tyy}: MPa	tan Φ_{xx}: dimensionless	tan Φ_{yy}: dimensionless	c_u: MPa
4·5	4·0	0·5	0·2	c_u/f_{txx}	c_u/f_{tyy}	0·2

f_{cxx} (f_{cyy}), masonry compressive strength along the x (y)-axis; f_{txx} (f_{tyy}), masonry tensile strength along x (y)-axis; c_u, pure shear strength; Φ_{xx} (Φ_{yy}), friction angle along the x (y) direction

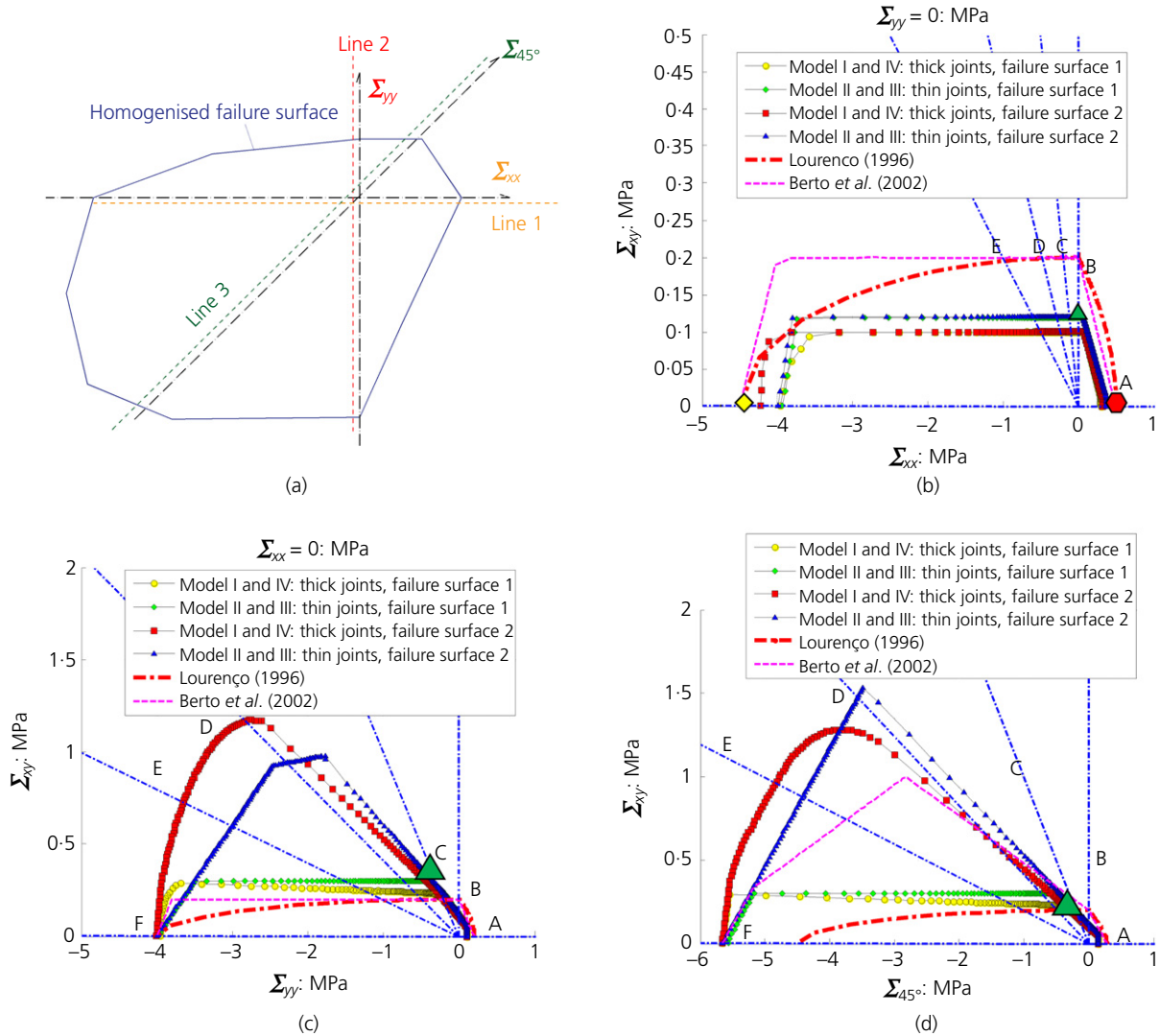**Table 3.** Mechanical properties adopted in the last set of numerical simulations

Figure 16. Homogenised failure surface sections along lines 1, 2, 3: (a) assuming for joints the strength domains reported in Figure 15; (b) $\Sigma_{yy} = 0$; (c) $\Sigma_{xx} = 0$; and (d) $\Sigma_{xx} = \Sigma_{yy}$

one for thick joints. As can be noted, there are some non-negligible differences among the results obtained with the first and second failure surfaces considered in Figure 15, and also the effect of the reduction of the joint to an interface modifies rather visibly the failure surface, consider for instance Figure 16(c) and the first failure surface.

The most relevant outcome of the comparison is, however, the inaccuracy of the macroscopic orthotropic models, especially along section lines 1 and 3, even in comparison with the homogenised failure surfaces obtained assuming for joints the second strength domain (i.e. with Tresca cut-off).

It should be therefore pointed out that particular care is required when macroscopic approaches are utilised, because in some cases they should provide incorrect evaluations of masonry strength along some directions of the load applied.

8. Conclusions

A detailed set of comparisons among homogenised running bond masonry strength domains provided by four different homogenisation models has been discussed. The first two procedures are lower bounds, whereas the last two approaches are upper bounds.
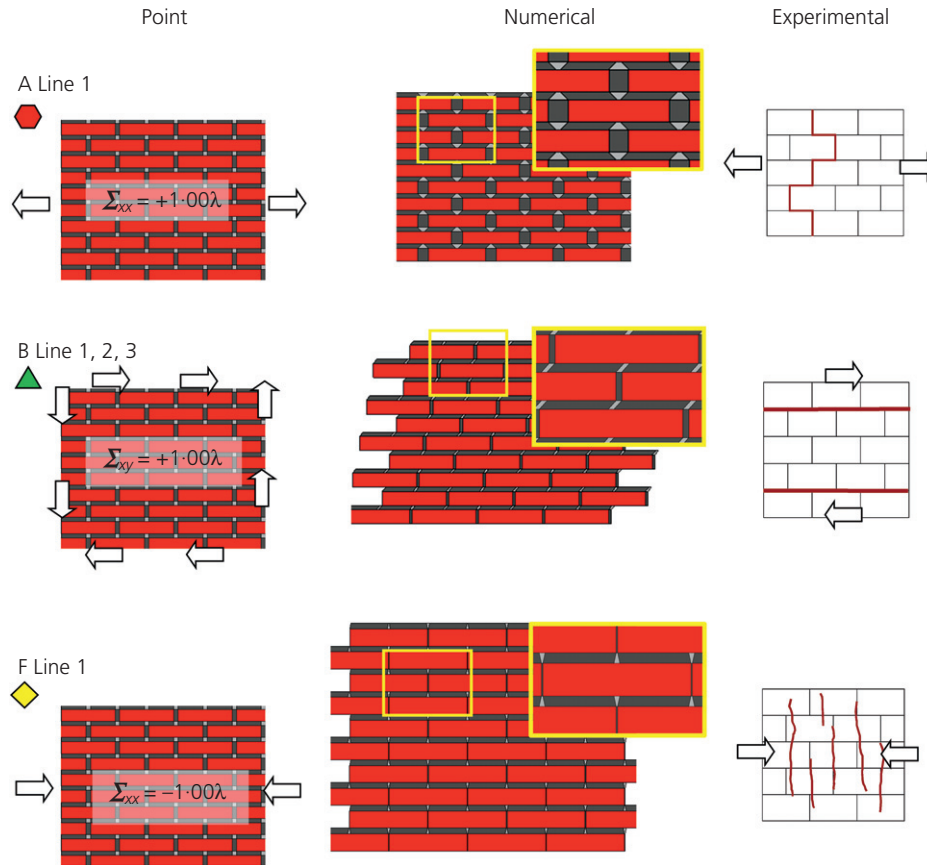
Figure 17. Comparison between numerical and experimentally observed failure modes for some meaningful points of the strength domain of Figure 16

In the first model, the elementary cell is subdivided into a few rectangular sub-domains, where the micro-stress field is expanded using polynomial expressions. Four polynomial expansions are presented (P0, P2, P3 and P4). P3 and P4 proved good convergence to either the actual solution in the case of joints reduced to interfaces or alternative upper bound approaches (MoC) and FEM in the case of thin joints. The second is again a lower bound, where joints are reduced to interfaces and bricks are subdivided into a few CST. The third procedure is a compatible identification, – that is an upper bound, where joints are reduced to interfaces and bricks are assumed infinitely resistant. The last model, MoC, is again a kinematic procedure where the elementary cell is subdivided into six rectangular sub-cells with pre-assigned polynomial fields of periodic velocity. The first and latter models have the advantage that allow the study of masonry with thick joints. A detailed comparison on results provided by all models has been discussed in the paper for a couple of cases of technical interest, focusing in particular on the role played by joint thickness, constituent materials failure surfaces and numerical efficiency, putting in evidence also the intrinsic limitations of the single approaches.

The original contribution of the present work is to put together four simple models coming from different sources, in single, ready-to-use software. The purpose is practical, and an open source version of the software will be available soon in a dedicated platform (as for instance SoftwareX) for free downloading at academic and professional levels. In this way, the comprehensive code allows a reliable and fast estimate of masonry failure surfaces with different approaches (upper and lower bounds), as well as a quantitative evaluation of the effect on the homogenised strength domain of the different hypotheses done on the constitutive behaviour of both mortar and bricks and on the thickness of the joints (reduction or not to interfaces).

In conclusion, it is stressed how, thanks to the very limited number of variables involved, the utilisation of the discussed 'direct' methods to estimate the ultimate behaviour of masonry through homogenisation is much more efficient with respect to both incremental elasto-plastic approaches and direct limit analysis FEM discretisation of the elementary cell.

REFERENCES

Aboudi J (1991) *Mechanics of Composite Materials: A Unified Micromechanical Approach*. Elsevier, Amsterdam, the Netherlands, Studies in Applied Mechanics, vol. 29.

Addessi D and Sacco E (2014) A kinematic enriched plane state formulation for the analysis of masonry panels. *European Journal of Mechanics A/Solids* **44(1)**: 188–200.

Berto L, Saetta A, Scotta R and Vitaliani R (2002) An orthotropic damage model for masonry structures. *International Journal for Numerical Methods in Engineering* **55(2)**: 127–157.

Casapulla C and Portioli F (2015) Experimental and analytical investigation on the frictional contact behavior of 3D masonry block assemblages. *Construction and Building Materials* **78(1)**: 126–143.

Cecchi A and Milani G (2008) A kinematic FE limit analysis model for thick English bond masonry walls. *International Journal of Solids and Structures* **45(5)**: 1302–1331.

Cecchi A, Milani G and Tralli A (2007) A Reissner–Mindlin limit analysis model for out-of-plane loaded running bond masonry walls. *International Journal of Solids and Structures* **44(5)**: 1438–1460.

de Buhan P and de Felice G (1997) A homogenisation approach to the ultimate strength of brick masonry. *Journal of the Mechanics and Physics of Solids* **45(7)**: 1085–1104.

Gilbert M, Casapulla C and Ahmed HM (2006) Limit analysis of masonry block structures with non-associative frictional joint using linear programming. *Computers and Structures* **84(13–14)**: 873–887.

Lotfi HR and Shing PB (1994) Interface model applied to fracture of masonry structures. *Journal of Engineering Mechanics ASCE* **120(1)**: 63–80.

Lourenço PB (1996) *Computational Strategies for Masonry Structures*. PhD thesis, Delft University of Technology, Delft, the Netherlands.

Lourenço PB and Rots J (1997) A multi-surface interface model for the analysis of masonry structures. *Journal of Engineering Mechanics ASCE* **123(7)**: 660–668.

Lourenço PB, de Borst R and Rots JG (1997) A plane stress softening plasticity model for orthotropic materials. *International Journal for Numerical Methods in Engineering* **40(21)**: 4033–4057.

Luciano R and Sacco E (1997) Homogenisation technique and damage model for old masonry material. *International Journal of Solids and Structures* **34(24)**: 3191–3208.

Milani G (2009) Homogenized limit analysis of FRP-reinforced masonry walls out-of-plane loaded. *Computational Mechanics* **43(5)**: 617–639.

Milani G (2011a) Simple homogenization model for the non-linear analysis of in-plane loaded masonry walls. *Computers and Structures* **89(17–18)**: 1586–1601.

Milani G (2011b) Simple lower bound limit analysis homogenization model for in- and out-of-plane loaded masonry walls. *Construction and Building Materials* **25(12)**: 4426–4443.

Milani G and Taliercio A (2015) In-plane failure surfaces for masonry with joints of finite thickness estimated by a method of cells-type approach. *Computers and Structures* **150(1)**: 34–51.

Milani G, Lourenco PB and Tralli A (2006a) Homogenised limit analysis of masonry walls, part I: failure surfaces. *Computers and Structures* **84(3–4)**: 166–180.

Milani G, Lourenco PB and Tralli A (2006b) Part II: structural examples, homogenised limit analysis of masonry walls, part II: structural examples. *Computers and Structures* **84(3–4)**: 181–195.

Milani G, Lourenco PB and Tralli A (2006c) Homogenization approach for the limit analysis of out-of-plane loaded masonry walls. *Journal of Structural Engineering ASCE* **132(10)**: 1650–1663.

Pegon P and Anthoine A (1997) Numerical strategies for solving continuum damage problems with softening: application to the homogenisation of masonry. *Computers and Structures* **64(1–4)**: 623–642.

Portioli F, Casapulla C, Cascini L, D'Aniello M and Landolfo R (2013) Limit analysis by linear programming of 3D masonry structures with associative friction laws and torsion interaction effects. *Archives of Applied Mechanics* **83(10)**: 1415–1438.

Portioli F, Casapulla C, Gilbert M and Cascini L (2014) Limit analysis of 3D masonry block structures with non-associative frictional joints using cone programming. *Computers and Structures* **143(1)**: 108–121.

Restrepo-Vélez LF, Magenes G and Griffith MC (2014) Dry stone masonry walls in bending-part I, static tests. *International Journal of Architectural Heritage* **8(1)**: 1–28.

Sahlaoui R, Sab K and Heck JV (2011) Yield strength of masonry-like structures containing thin adhesive joints: 3D or 2D-interface model for the joints? *Comptes Rendus Mecanique* **339(6)**: 432–438.

Shieh-Beygi B and Pietruszczak S (2008) Numerical analysis of structural masonry: mesoscale approach. *Computers and Structures* **86(21–22)**: 1958–1973.

Stefanou I, Sab K and Heck JV (2014) Three dimensional homogenization of masonry structures with building blocks of finite strength: a closed form strength domain. *International Journal of Solids and Structures* **54(1)**: 258–270.

Suquet P (1983) Analyse limite et homogeneisation. *Comptes Rendus de l'Academie des Sciences – Series IIB – Mechanics* **296(18)**: 1355–1358.

Taliercio A (2014) Closed-form expressions for the macroscopic in-plane elastic and creep coefficients of brick masonry. *International Journal of Solids and Structures* **51(17)**: 2949–2963.

Vasconcelos G and Lourenço PB (2009) Experimental characterization of stone masonry in shear and compression. *Construction and Building Materials* **23(11)**: 3337–3345.